



HAL
open science

The Archean Pavas Block in Uruguay: Extension and tectonic evolution based on LA-ICP-MS U–Pb ages and airborne geophysics

Henri Masquelin, Tahar Aïfa, Fernando Scaglia, Miguel a S Basei

► To cite this version:

Henri Masquelin, Tahar Aïfa, Fernando Scaglia, Miguel a S Basei. The Archean Pavas Block in Uruguay: Extension and tectonic evolution based on LA-ICP-MS U–Pb ages and airborne geophysics. *Journal of South American Earth Sciences*, 2021, 110, pp.103364. <10.1016/j.jsames.2021.103364>. <insu-03233680>

HAL Id: insu-03233680

<https://insu.hal.science/insu-03233680v1>

Submitted on 25 May 2021

HAL is a multi-disciplinary open access archive for the deposit and dissemination of scientific research documents, whether they are published or not. The documents may come from teaching and research institutions in France or abroad, or from public or private research centers.

L'archive ouverte pluridisciplinaire HAL, est destinée au dépôt et à la diffusion de documents scientifiques de niveau recherche, publiés ou non, émanant des établissements d'enseignement et de recherche français ou étrangers, des laboratoires publics ou privés.



HAL Authorization

Journal Pre-proof

The Archean Pavas Block in Uruguay: Extension and tectonic evolution based on LA-ICP-MS U–Pb ages and airborne geophysics

Henri Masquelin, Tahar Aïfa, Fernando Scaglia, Miguel A.S. Basei



PII: S0895-9811(21)00211-X

DOI: <https://doi.org/10.1016/j.jsames.2021.103364>

Reference: SAMES 103364

To appear in: *Journal of South American Earth Sciences*

Received Date: 27 July 2020

Revised Date: 31 March 2021

Accepted Date: 27 April 2021

Please cite this article as: Masquelin, H., Aïfa, T., Scaglia, F., Basei, M.A.S., The Archean Pavas Block in Uruguay: Extension and tectonic evolution based on LA-ICP-MS U–Pb ages and airborne geophysics, *Journal of South American Earth Sciences* (2021), doi: <https://doi.org/10.1016/j.jsames.2021.103364>.

This is a PDF file of an article that has undergone enhancements after acceptance, such as the addition of a cover page and metadata, and formatting for readability, but it is not yet the definitive version of record. This version will undergo additional copyediting, typesetting and review before it is published in its final form, but we are providing this version to give early visibility of the article. Please note that, during the production process, errors may be discovered which could affect the content, and all legal disclaimers that apply to the journal pertain.

© 2021 Published by Elsevier Ltd.

The Archean Pavas Block in Uruguay: extension and tectonic evolution based on LA-ICP-MS U-Pb ages and airborne geophysics

Henri Masquelin ^{1,*}, Tahar Aïfa ², Fernando Scaglia ³, Miguel A.S. Basei ⁴

1 – Instituto de Ciencias Geológicas, Facultad de Ciencias – UdelaR, Iguá 4225 p12 ala sur,
11400 Montevideo, Uruguay

2 – Univ. Rennes, CNRS, Géosciences Rennes – UMR6118, Campus Beaulieu, 35042 Rennes, France

3 – Post-graduate Course, PEDECIBA Geosciences, Uruguay

4 – Centro de Pesquisas Geocronológicas, Universidade de São Paulo, Brazil

*emasquelin@fcien.edu.uy

Abstract

The Pavas Block is an Archean/Paleoproterozoic inlier located in the central segment of Uruguay's Precambrian exposition. A new insight initiated due to the acquisition of airborne geophysical data and new U-Pb zircon dating. The correlation of Archean crustal inliers in the amalgamation of the South American Platform is one of the main objectives in the Precambrian geological investigation. Although Ediacaran lateral strike-slip shear zones controlled the Pavas Block, their ultimate boundaries are not clear. Furthermore, a pre-Neoproterozoic metasedimentary succession discordant on this block is often confused with Neoproterozoic ones. Correctly identifying these limits is a necessary task to modify wrong tectono-stratigraphic models. The airborne total count radiometric imaging and the horizontal derivative of the total magnetic field anomaly reduced to the pole at 1000 m elevation led to establishing the Pavas Block's dimensions, based on new structural interpretation. The filtered magnetic anomaly is concordant with the previous Bouguer anomaly indicating a westward virgation of the Pavas Block in the north. This inlier narrows through the Minas city and along the Sarandí del Yí shear zone. The Sierra de Sosa and Sierra Ballena shear zones were confirmed as lateral limits. The total count radiometric map highlights the presence of brittle-fault reactivation. The Archean La China Complex containing zircons from three periods (~3.3-3.1 Ga; 3.0; 2.8-2.7 Ga) is in the Pavas Block's centre. New U-Pb zircon geochronology provided six samples from different metagranitoids that yielded LA-ICPMS U-Pb zircon ages ranging between 3353±9 Ma and 1839±2 Ma. Its southern periphery shows more recent Archean and Orosirian metagranitoids. These rocks were later partially affected by Neoproterozoic deformation. The preservation of igneous textures, field relationships, and zircon textures suggested that younger Neoarchean intrusive granitoids emplaced within the basal granitic gneiss "La China" complex. The pre-Neoproterozoic metasedimentary cover intercalates with Neoproterozoic successions until the southern end of the Pavas Block against the Sarandí del Yí Shear Zone. Finally, one granitoid devoid of Archean inherited zircons yielded a concordant ²⁰⁷Pb/²⁰⁶Pb zircon age of 1999±3 Ma (MSWD=8.1) interpreted as magmatic crystallisation. This Orosirian K-feldspar granite is likely to set the southern border of the block in a transitional crust. The Pavas Block is limited from the Villa Serrana Block by a schist belt of Mesoproterozoic protoliths, and reports enough information to be interpreted as a suspect terrane.

Keywords: Precambrian, Zircon texture, Granitic Gneiss, Nico Perez Terrane, Gamma Spectrometry.

39 1. INTRODUCTION

40 The Pavas Block is a small (i.e., 3000 km²), elongated Archean/Paleoproterozoic inlier located in the
41 centre of the Nico Pérez Terrane of central Uruguay (Preciozzi et al., 1979, 1985; Masquelin, 2006;
42 Sánchez Bettucci et al., 2010; Oriolo et al., 2016a; Oyhantçabal et al., 2018; Fig. 1). The Nico Pérez
43 Terrane (NPT) of Uruguay is part of the West-Gondwana Neoproterozoic amalgamation (Brito Neves et
44 al., 1999; Campos Neto, 2000). This crustal segment forms an acute triangle, limited to the eastern Rio de
45 la Plata Craton by the Sarandí del Yí shear zone and the western terrane by the Sierra Ballena Shear Zone
46 (Bossi and Campal, 1992; Oriolo et al., 2016a, b).

47 The definition of minor entities like the Cerro Chato and Pavas sub-terrane (Oyhantçabal et al., 2018) or
48 blocks (Oriolo et al., 2019) is not new (e.g., Preciozzi et al., 1979; Masquelin, 2006). However, this
49 scheme provides new insight into the structural framework of the Precambrian in central Uruguay in the
50 light of new geochronological and geophysical data. So far, the Pavas Block is the only one exposing
51 Archean rocks in the NPT (Hartmann et al., 2001; Mallmann et al., 2007). However, the isotopic
52 inheritance reveals that Archean sources are widespread in the whole Nico Pérez Terrane (Oyhantçabal et
53 al., 2018). Archean inheritance was verified in the TDM model ages Sm-Nd and Lu-Hf in zircon (Babinski
54 et al., 1997; Hartmann et al., 1999; Santos et al., 2003; Mallmann et al., 2007; Oyhantçabal et al., 2011,
55 2018; Oriolo et al., 2015, 2016a; Lara et al., 2020). Likewise, the metamorphic zircons show a U-Pb
56 system that registers robust Archean inheritance in all the analyses (Hartmann et al., 2001; Gaucher et al.,
57 2011; Oyhantçabal et al., 2012; Oriolo et al., 2019). The detrital provenance of the metamorphic cover
58 succession shows Archean age peaks that strongly contrast with the ages of the Rio de la Plata Craton
59 (Blanco et al., 2009; Peçoits et al., 2016; Oyhantçabal et al., 2021).

60 The Pavas Block's extension is of principal interest due to the suspicion of a terrane accretion model to
61 test a theory presented in some recent works (Rapela et al., 2011; Girelli et al., 2018). The whole NPT was
62 initially interpreted as a Neoproterozoic tectonostratigraphic "suspected" terrane separated through ductile
63 shear zones (Bossi and Gaucher, 2004). Ambiguity revolves around whether the tectonic events
64 responsible for the updated structural framework reflect intra-plate (intra-cratonic) processes or those
65 linked to and driven by interactions at plate margins (e.g., Clark et al. 2007). The primary character of
66 crustal blocks in an orogenic collage must distinguish itself from their late-orogenic secondary framework
67 (Şengör and Dewey, 1990; Fernandes et al., 1995; De Toni et al., 2021). Tectonic models of Precambrian
68 orogens either miss the existence of large brittle faults or mistake them for ductile shear zones. The
69 inaccuracies in the description of lithostratigraphic terranes or blocks apply to the NPT. Therefore, the
70 structural analysis needs to point towards definitions of different meanings. High-resolution airborne
71 geophysics would make it possible to underpin these definitions. Likewise, high- accuracy airborne
72 magnetic and radiometric data is a powerful tool for scrutinising brittle faults and their kinematic
73 indicators.

74 The Pavas and Congo-Chato Blocks represent the western foreland basement of the Dom Feliciano Belt
75 (DFB; Basei et al., 2000; Masquelin, 2006; Sánchez-Bettucci et al., 2010; Oyhantçabal et al. 2011b;
76 Philipp et al., 2016; Peel et al., 2018; Hueck et al., 2018; Oriolo et al., 2019). A curved discontinuity
77 called the Sierra de Sosa Transcurrent System separated both blocks (Campal and Schipilov, 1999; Bossi
78 et al., 2001). The discontinuity is also known as the Cueva del Tigre or Sierra de Sosa strike-slip shear
79 zone (Masquelin, 2006; Gaucher et al., 2014a; Oyhantçabal et al., 2018).

80 The Pavas Block is made up of a basal granitic gneiss, probably derived from magmatic TTG Suites, and a
81 medium to high-grade metamorphic cover sequence (Hartmann et al., 2001). One question that arises is to
82 quantify the full exposition of the Archean rocks and their boundaries, especially through its southern
83 edge, and its relationship with the southernmost Villa Serrana Block (Bossi and Gaucher, 2004).

84 Another question concerns the different degrees of tectono-thermal recycling of the Archean crust and the
85 geological records that are evidencing a Rhyacian-Orosirian multi-episodic tectonic evolution
86 (Oyhantçabal et al., 2012, 2018). The lithological correlation between the Pavas Block and the Congo-São
87 Francisco Craton can help the geotectonic reconstructions concerning the geology of the pre-
88 Neoproterozoic cover sequence, named the Las Tetras Complex (Hartmann et al., 2001). Locally, the Las
89 Tetras Complex indicates a much broader and interspersed distribution towards the south (until the Minas
90 city). The São Francisco Craton reported another metamorphic association composed of oligomictic
91 quartz-conglomerates, fuchsite-sillimanite quartzites, amphibolites, micaschists, stromatolitic carbonatic
92 rocks, and BIF (Oliveira et al., 2002; Milési et al., 2002; Rosière et al., 2018). Chromium-rich
93 hydrothermalism that altered Pre-Neoproterozoic rocks is common in many cratonic regions worldwide
94 (e.g., Nutman et al., 2014; Sing and Slabunov, 2016; Kielman et al., 2018; Albert et al., 2018). Together
95 with their isotopic fingerprints or signatures (Scherer et al., 2007; Harley et al., 2007; Pearce et al., 2014;
96 Grimes et al., 2015; Roberts and Spencer, 2015), they could be a powerful tool to make correlations like
97 those pointing to the Columbia Paleo-continent's reconstructions (e.g., Girelli et al., 2018; Bruno et al.,
98 2021).

99 This study aims to revise the Pavas Block's extension towards the south and its lateral boundaries. This
100 work attempts to (i) discuss their boundaries, using airborne magnetic and total count radiometric data,
101 and (ii) discriminate Archean-recycled to non-recycled rocks. For this purpose, we have used the U-Pb age
102 correlation from six new laser ablation ICP-MS U-Pb zircon analyses. Zircon textural features and
103 petrography are essential tools to contextualise geochronological data. All zircons studied come from
104 high-to-medium grade metamorphic rocks of the La China Complex (Hartmann et al., 2001) and the
105 Campanero Unit (Sánchez Bettucci et al., 2003).

106 **2. GEOLOGICAL SETTING**

107 ***2.1. Local setting and boundaries of the Pavas Block***

108 The discovery of the "Pavas Formation" initiated as a photointerpretation recognising contrasted
109 geomorphology and lithological associations (Preciozzi et al., 1979). The exposing area is located between

110 the Sierra de Sosa and the Mata Abonia shear zones (Bates et al., 2016; Oriolo et al., 2016a, Sánchez
111 Bettucci et al., 2021). The block has been mapped as a narrow band of 20 km wide and 200 km in length
112 on average (most extensive to the North: 32 km), oriented NE-SW between latitudes -33.78° and -32.80°
113 (Fig. 1c) (Preciozzi et al., 1985; Gaucher et al., 2014a; Oriolo et al., 2019). The revised Bouguer anomaly
114 map of Uruguay (Rodríguez et al., 2015) shows a critical positive anomaly at the north-eastern corner of
115 this area. The magnetotelluric profile indicates that the Pavas and Cerro Chato blocks both have a 200
116 kilometre's thickness, which is inherited from a cratonic setting (Bologna et al., 2019). In geological
117 maps, the block's shape seems controversial, depending on how different authors interpreted their
118 boundary faults (e.g., Preciozzi et al., 1979; Sánchez Bettucci et al., 2010; Oyhantçabal et al., 2021). Some
119 sketches place an eastward convexity for the western limit, called the Cueva del Tigre Fault (Preciozzi et
120 al., 1979). Others place a westward convexity, giving the block a spindle shape (e.g., Bossi et al., 2001;
121 Mallmann et al., 2007; Sánchez Bettucci et al., 2010). The Tupambaé shear zone is its northern limit
122 (Bates et al., 2016). Southward, the NW-SE striking Santa Lucia granite truncated it. Eastward, it limits
123 through the Puntas de Pan de Azúcar shear zone (Guerrero et al., 2016) and the Sierra Ballena shear zone
124 as the last resort (Hartmann et al., 2001). This definition mostly concerns the basal granitic-gneissic
125 complex because many "flakes" of the Neoproterozoic metamorphic cover succession extend beyond the
126 contact of the inner granitic-gneissic nucleus (Fig. 2) (e.g., Oriolo et al., 2016a; Oyhantçabal et al., 2021).
127 Most interpretations have in common that the Sierra de Sosa shear zone represents the western boundary
128 (Campal and Schipilov, 1999; Bates et al., 2016; Oriolo et al., 2016a). Many geologic maps place thrusts
129 dipping to the NW, others to the SE, but none present structural measurements at the 1:500,000 scale to
130 sustain this information.

131 **2.2. Geotectonic location**

132 The Archean block is in the central segment of the Precambrian exposition in Uruguay called the "Nico
133 Pérez Terrane" (NPT; Bossi and Campal, 1991, 1992; Oriolo et al., 2016a; Fig. 1). The NPT locates
134 between the Rio de la Plata Craton (Almeida et al., 1973) and the Aiguá - Pelotas Batholith (Masquelin,
135 2006). Together with the DFB, this tectonic wedge represents part of the Brasiliano orogenic collage (e.g.,
136 Şengör and Dewey, 1990) named the Mantiqueira Province in Brazil (Hasui et al., 1982; Jost and
137 Hartmann, 1984; Da Silva et al., 2005). This part of the South American Platform includes many inliers of
138 different ages and histories, which took place in Late Proterozoic times (Brito Neves and Cordani, 1991;
139 Campos Neto, 2000; Brito Neves et al., 2014). The Mantiqueira province was already known as having an
140 "Archean structure" and a Proterozoic evolution that combined two terranes' kinds, (i) granulitic and (ii)
141 granitic-gneissic with supracrustal relics (Hasui et al., 1982). Some inliers are cratonic, and others are
142 "fertilised" (Bologna et al., 2019). The final structure developed after a protracted Neoproterozoic
143 amalgamation of major crustal blocks and branched systems of orogenic belts (Brito Neves et al., 2014). It
144 gave rise to the Western Gondwana accretion after the Rodinia breakup (Cordani et al., 2003).
145 Furthermore, the Pavas Block also represents basement rocks involved in the foreland of the
146 Neoproterozoic Dom Feliciano Belt (DFB; Fragozo Cesar, 1980; Fernandes et al., 1995; Basei et al., 2000;

147 Oyhançabal et al., 2009, 2018; Oriolo et al., 2016a, c; Hueck et al., 2018; Masquini et al., 2017; Lara et
148 al., 2020). These basement rocks were affected by Neoproterozoic metamorphism, deformation, and
149 granitic magmatism (Oriolo et al., 2016a, c; Hueck et al., 2018). The degree of recycling is variable
150 depending on each block. The DFB has been correlated with the Kaoko and Gariep Belts of southwestern
151 Africa. All of them show a similar tectono-magmatic evolution during the Pan-African/Brasiliano
152 orogenesis (Basei et al., 2008; Goscombe and Gray, 2007; Frimmel et al., 2011; Hueck et al., 2018 and
153 references therein).

154 **2.3. Geotectonic evolution**

155 The juxtaposition of the Río de la Plata, Kalahari, and Congo Cratons together with other continental
156 fragments such as the Pavas Block and the Luiz Alves Terrane took place to form the Western Gondwana
157 (Basei et al., 2005; Goscombe et al., 2005; Gray et al., 2008). The first cause of structural complexity in
158 the Mantiqueira Province and the Dom Feliciano Belt (DFB) is that penetrative strike-slip shear zones
159 usually juxtapose sectors with no connection in the transversal section (e.g., Burke and Şengör, 1986). The
160 last Neoproterozoic tectonic event, associated with the Sierra Ballena strike-slip shear zone, was
161 transpressive (Oyhantçabal et al., 2009, 2011; Oriolo et al., 2016b). It was probably followed by lateral
162 escape, although the “indentor” is not clear (Fernandes et al., 1993; Tommasi et al., 1994). The
163 Neoproterozoic magmatic activity in the NPT included the last emplacement of late-orogenic granites
164 (~600-580 Ma), channelizing through shear zones (e.g., Fort, 2020; Lara et al., 2020). The Pavas Block
165 can be considered an inlier that survived from both the Paleoproterozoic recycling and the Brasiliano/Pan-
166 African tectono-thermal event. Therefore, the whole NPT was postulated as a Congo Craton fragment
167 (Oriolo et al., 2016a; Oyhançabal et al., 2018).

168 An integrated tectonic evolution suggests that NPT's Archean crust underwent magmatic accretion and
169 recycling during Rhyacian and Orosirian tectono-metamorphic events (Santos et al., 2003; Oyhançabal et
170 al., 2012). The Rhyacian event recorded magmatism at ca. 2.2-2.1 Ga followed by high-grade
171 metamorphism associated with crustal anatexis at ca. 2.1-2.0 Ga (Oyhantçabal et al., 2012; Oriolo et al.,
172 2016a; Girelli et al., 2018). This first amalgamation underwent a polyphase deformation during the
173 collision between the Kalahari and the Congo-Rio de la Plata plates in the interval 650-600 Ma (Fernandes
174 et al., 1992; Oriolo et al., 2016a; Hueck et al., 2018). This protracted evolution could involve a suspected
175 terrane accretion process (Rapela et al., 2011). In this case, amalgamation's driving mechanism is not
176 obvious because the crustal growth might occur in an environment of long-term subduction and plate
177 convergence without the collision of large continental blocks (Murphy and Nance, 1991; Cawood and
178 Buchan, 2007).

179 **2.4. Regional age constraints**

180 Absolute age constraints presented here cover the entire Nico Pérez Terrane. Sm-Nd TDM model ages
181 were treated in general. Such U-Pb in zircon combined with other methods) are treated in detail. The U-Pb

182 samples are shown in the geological map (Fig. 2). Table I and III displays all the U-Pb results, collected
183 and antecedent (Annexe 1, Data-In-Brief).

184 2.4.1. Sm-Nd and Lu-Hf TDM-model ages

185 Although Sm-Nd and Lu-Hf TDM-model ages and zircon inheritance in NPT reflect dominant
186 Paleoproterozoic sources, they also indicate the ubiquitous presence of an Archean precursor (Santos et al.
187 2003; Mallmann et al. 2007; Oyhantçabal et al., 2021; Oriolo et al. 2016a; Lara et al., 2020). Based on the
188 TDM (Nd) and (Hf) model-ages, Oyhantçabal et al. (2012) suggested a polycyclic evolution initiating in
189 the Archean. Southern Neoproterozoic granites (~596-610 Ma) of the Villa Serrana Block and the Aiguá
190 Batholith (Fig. 2) gives an evolved Sr and Nd isotopic signatures ($^{87}\text{Sr}/^{86}\text{Sr}_i$ of 0.708; negative ϵNd of -14
191 to -20). An Nd-TDM model age is in the interval ~2.3-2.8 Ga. Their zircons yield a negative $\epsilon\text{Hf}(t)$ (-21 to
192 -27) but Hf model ages of ~3.6 Ga (Lara et al. 2020). Archean inherited components also appear in the
193 northern Neoproterozoic granites (~619 Ma) (Fig. 2). Zircons show Hf model ages of 2.69 and 2.59 Ga,
194 respectively (Fort, 2020). Both results confirm Archean precursors' widespread occurrence westward
195 along the Sierra Ballena Shear Zone (Oyhantçabal et al., 2018). In the Villa Serrana Block (Fig. 2), the
196 mylonitic syenogranite (sample NP-154; Table I, Annexe 1) shows an Nd-TDM of 2.84 Ga, indicating an
197 Archean mantellic extraction for the source (Mallmann et al., 2007). Detrital zircon ages collected in
198 metasediments of the Zanja del Tigre Complex (Fig. 2) yielded (i) Paleoproterozoic ages of 2.18 to 1.96
199 Ga, and (ii) Archean ages of 3.54 to 2.67 Ga (Mallmann et al., 2007).

200 2.4.2. Rhyacian / Orosirian evolution based on the Th-U-Pb system

201 The complete Paleoproterozoic evolution is documented in Rivera and Cerro Chato blocks (Fig. 1c).
202 Using combined geochronological methods, as SHRIMP U-Pb zircon, Th-U-Pb monazite (CHIME -
203 EPMA method) and K-Ar (W-R and amphibole), the resulted evolution recorded (i) Rhyacian magmatism
204 at 2.17-2.11 Ga, and (ii) Orosirian granulite-facies anatexis event, at ~2.08 Ga (on zircon overgrowths),
205 and the metamorphic thermal peak at ~1.98 Ga in monazite (Oyhantçabal et al., 2012; Table III; Annexe
206 1).

207 Zircons extracted from metagranitoids of the Valentines region (Fig. 2) yielded U-Pb zircon (SHRIMP)
208 ages of ~2.2 Ga. These zircons show some Neoproterozoic (~2.7 Ga) inherited euhedral cores with oscillatory
209 zoning (Santos et al., 2003; Oriolo et al., 2016a; Table III, Annexe 1). Oscillatory zoning pattern (OZP) is
210 also present in the rims. Zircon cores yielded a weighted mean $^{206}\text{Pb}/^{238}\text{U}$ age of 2106 ± 21 Ma (MSWD of
211 concordance = 3.2) interpreted as the igneous crystallisation age. Meanwhile, some rims yielded an age of
212 ~600 Ma, interpreted as the Neoproterozoic metamorphism with anatexis (Santos et al., 2003; Table III,
213 Annexe 1). The $^{207}\text{Pb}/^{206}\text{Pb}$ age of 2057.5 ± 2.8 Ma (MSWD = 0.96) (n=6) was interpreted as the age of
214 metamorphic recrystallisation. Unzoned overgrowth rims pointed to a granulite facies anatexis event
215 (~2.0 Ga).

216 A Statherian tectono-thermal event was reported in the southernmost Villa Serrana Block (Fig. 2). The
217 Campanero Unit constitute the gneissic rocks of the Paleoproterozoic basement in this region (Sánchez

218 Detrucci et al., 2005). A syenogranite (sample 0198, Table III, Annexe 1) yielded the first U-Pb
219 conventional dating giving a Discordia upper intercept age of $1735 \pm 32 \pm 17$ Ma and interpreted as
220 magmatic crystallisation. Meanwhile, the authors explained the lower intercept age ($723 \pm 240 \pm 210$ Ma) as
221 due to Neoproterozoic deformation. Meanwhile, they interpreted the 1754 ± 6.8 Ma upper intercept age as
222 magmatic crystallisation. Granitic plutons of 1.8-1.7 Ga, like the Illescas granite in the Cerro Chato Block
223 (Fig. 2), are typically post-orogenic concerning the Orosirian orogenesis (~ 2.0 Ga). Despite presenting a
224 Brasiliano mylonitization, these granites were correlated with the Illescas granite based on their Rb-Sr and
225 U-Pb age (Campal and Schipilov, 1995; Oriolo et al., 2019).

226 The Rhyacian/Orosirian evolution can be correlated with the Camboriú (Da Silva et al., 2005) and Santa
227 Maria Chico complexes (Tickyj et al., 2004; Girelli et al., 2018), as both reported the ages mentioned
228 above. Girelli et al. (2018) pointed out that the granulite facies metamorphic event at ~ 2.06 Ga was at the
229 onset of multi-accretional terranes' amalgamation against the Rio de la Plata Craton (RPC).

230 2.4.3. Geochronology in the Pavas Block

231 The Pavas Block contains metagranitoids displaying Neo to Meso-Archean metamorphic ages obtained by
232 the U-Pb zircon (SHRIMP) method (Hartmann et al., 2001; Gaucher et al., 2011). Hartmann et al. (2001)
233 separated two events at 3.41-3.15 Ga (magmatism and recrystallisation) and 2.76 Ga (Pb-loss by
234 deformation). The first dated orthogneiss yields zircon cores reaching a U-Pb SHRIMP age of 3404 ± 8
235 Ma (Hartmann et al., 2001). This age was interpreted as magmatic crystallisation. In contrast, slightly
236 younger ages (~ 3.1 Ga) in the zircon rims were interpreted as partial resetting due to an upper amphibolite
237 facies metamorphism. Gaucher et al. (2011) obtained a new U-Pb LA-ICP-MS zircon age of 3096 ± 45
238 Ma near the first dating place and interpreted it as partial melting crystallisation. Gaucher et al. (2014a)
239 presented a new SHRIMP U-Pb zircon age from a mylonitic granitoid (sample FZ6; Table III, Annexe 1)
240 that yielded a $^{207}\text{Pb}/^{206}\text{Pb}$ magmatic crystallisation age of 2787 ± 6 Ma. Hartmann et al. (2001) suggested
241 that sectors having ~ 2.76 Ga were not affected by the Orosirian anatectic event (at ~ 2.07 Ga). On the other
242 hand, the minimum age of the detrital zircon provenance in the Las Tetras Complex is 2717 ± 24 Ma
243 (Hartmann et al., 2001). Oyhantçabal et al. (2021) confirmed that the Las Tetras Complex is characterized
244 by the lack of Proterozoic detrital zircon grains. Following these authors, the absence of
245 Rhyacian/Orosirian zircon grains is remarkable, despite this being the dominant age peak in all other units
246 of the NPT. A ca. 630-600 Ma metamorphic overprints this complex, constrained by Ar/Ar phlogopite and
247 muscovite data (Oriolo et al., 2016b). Neoproterozoic intrusions within the Pavas Block are represented by
248 the Zapicán diorite that emplaced parallel to the Sierra de Sosa shear zone. This late-kinematic diorite
249 yields a magmatic crystallisation age ($^{206}\text{Pb}/^{238}\text{U}$) of 610.4 ± 2.5 Ma (Oriolo et al., 2016a).

250 2.5. Main rock units and structures

251 The Pavas Block comprises the pre-Neoproterozoic La China Complex (Hartmann et al., 2001), as the
252 basement unit, and the Las Tetras metasediments, as a platform cover (e.g., Preciozzi et al. 1979, 1985;
253 Oyhantçabal and Vaz Chaves, 1990; Hartmann et al. 2001; Oriolo et al., 2016a; Masquelin et al., 2017;

254 Oyhantçabal et al., 2021). The contact between both complexes is tectonic, including thrusts and high
255 angle transcurrent shear zones (Campal and Schipilov, 1999; Hartmann et al., 2001; Bossi et al., 2001;
256 Oriolo et al., 2016a).

257 2.5.1. *The La China Complex*

258 The La China Complex contains felsic granitic-gneisses, amphibolites and ultramafic rocks generally
259 retrogressed to actinolite-schists, talc-schists, and serpentinites (Preciozzi et al. 1979, 1985; Hartmann et
260 al., 2001; Gaucher et al., 2014a; Oriolo et al., 2016a). A tonalite - trondhjemite - granodiorite (TTG)
261 affinity was assumed for these migmatitic orthogneisses, although no geochemistry emerges (Hartmann et
262 al., 2001; Gaucher et al., 2014a). The granitic gneisses recorded low angle layering and interspersed with
263 amphibolites. However, L-fabrics and a penetrative mineral lineation represent it, plunging at a low-angle
264 to the southwest or south (Oriolo et al., 2016b; Masquelin et al., 2017). The basal gneisses are variable
265 under the Ediacaran Barriga Negra formation (Masquelin et al., 2017; Núñez Demarco et al., 2018a, b). A
266 banded, fine-grained, muscovite-rich granitoid is common. Then it is crosscut first by white pegmatites
267 and then by a K-feldspar rich coarse-grained granitoid. Other sections show a flat-lying mylonitic rock
268 with a strong stretching lineation plunging towards the N-E. Low angle contact relationships with the
269 stretched meta-conglomerate, stratified sericite-schists and quartzites are visible (Núñez Demarco et al.,
270 2018b).

271 2.5.2. *The Las Tetas Complex*

272 The Las Tetas Complex is a medium-grade metamorphic succession composed of fuchsite-bearing meta-
273 conglomerates, quartzites, garnet - biotite micaschists, quartz-(tourmaline)-mica schists, marbles, black-
274 shales, BIF, garnet-bearing and garnet-free amphibolites (Oyhantçabal and Vaz 1990; Preciozzi et al.,
275 1988a, b; Hartmann et al. 2001; Gaucher et al. 2014b; Masquelin et al., 2017; Oyhantçabal et al., 2021). In
276 recent geological maps, this succession extends over the granitic-gneissic basement to the SBSZ (Oriolo et
277 al., 2019; Oyhantçabal et al., 2021). Sillimanite-bearing quartzites were described in the north
278 (Oyhantçabal and Vaz 1990), whereas staurolite-garnet micaschists were described in the south (Preciozzi
279 et al., 1989; Hartmann et al. 2001). Quartz-mica schists, quartzites and fuchsite-bearing meta-
280 conglomerates are interbedded and affected by upright folds (Oriolo et al., 2016b). Chevron folds and
281 kinks are common. Although no detrital zircons are available on stromatolitic carbonate successions, field
282 relationships suggest that these carbonates associate with the rest of the above-mentioned rocks. The
283 youngest detrital zircon age peak (n=16) of ~2764 Ma still constrains the maximum deposition age of Las
284 Tetas' succession (Hartmann et al. 2001; Oyhantçabal et al., 2021). A Neoproterozoic / Siderian deposition
285 age is likely because detrital zircons from the whole Proterozoic provenance are lack (Oyhantçabal et al.,
286 2021). This top provenance age is reinforced given the Orosirian age of the isotropic Arroyo Perdido
287 granite (near Minas), which crosscut the Las Tetas Complex. This granite yielded an Rb-Sr age of $2001 \pm$
288 117 Ma (Umpierre and Halpern, 1971; Gaucher et al., 2006), which were confirmed at 2036 ± 4 Ma by U-

289 U-Pb SHRIMP method (Gaucher et al., 2014b). The minimum age of recycling was constrained by a
290 $^{40}\text{Ar}/^{39}\text{Ar}$ age of 621.4 ± 1.0 Ma in phlogopite taken from the Polanco marbles (Oriolo et al. 2016b).
291 Its original basin could be a stable-shelf siliciclastic-carbonate platform (Hartmann et al., 2001). The Las
292 Tetras Complex is thrust-stacked and interspersed with the La China Complex rocks (Hartmann et al.,
293 2001; Gaucher et al., 2014b). Sillimanite indicates high-grade metamorphic/anatectic conditions above
294 600°C (Oyhantçabal and Vaz, 1990). The stretching lineation on quartz-clasts of the basal fuchsite-bearing
295 meta-conglomerate is $15^\circ/160^\circ$ (Masquelin et al., 2017; Núñez Demarco, 2018a, b, 2019). Despite the N-S
296 stretching, the meta-conglomerate still preserves bedding (Masquelin et al., 2017). The Polanco/Manguera
297 Azul marbles also show mineral lineations ($15^\circ/220^\circ$) and mineral assemblages coherent with upper
298 greenschist facies (Silva Lara et al., 2018).

299 2.5.3. Sierra de Sosa shear zone (SSSZ)

300 The Sierra de Sosa shear zone separates the Cerro Chato from the Pavas block. Campal and Schipilov
301 (1999) defined first the “Sierra de Sosa Transcurrent System”. This system involved strike-slip faults and
302 thrusts. The Sierra de Sosa Shear Zone (SSSZ) (Gaucher et al., 2014a) crosscut different lithologies and
303 presents a mean mylonitic foliation of $219^\circ/70^\circ$ and a mean stretching lineation of $15^\circ/225^\circ$ (Oriolo et al.,
304 2016b). The “transcurrent system” is made up of a 3-5 km wide strip, with a 020° orientation that extends
305 over tens of kilometres in length. Kilometre-wide protomylonitic Kfs-rich granitoids and vertical
306 mylonites are the main rocks (Campal and Schipilov, 1999). However, it also contains layered gneisses
307 and amphibolites. This lithological association suggests that initial conditions during the deformation were
308 linked to amphibolite facies. The mylonites contain “shreds” of carbonate rocks, green schists, and BIF
309 (Campal and Schipilov, 1999). Different authors recognise the dextral strike-slip at different scales (Bossi
310 et al., 2001; Masquelin et al., 2017). However, mesoscopic kinematic indicators like S-C shear bands and
311 δ - and σ -type feldspar mantled porphyroclasts indicate a sinistral shear (Oriolo et al., 2016b). The SSSZ
312 encounters the SYSZ at its southwestern limit. The Sierra de Sosa Shear Zone hosts protomylonitic K-
313 feldspar granites to the west. Finally, the SSSZ hosts the 030° striking, late-kinematic intrusion of the
314 Zapicán diorite, which yields a U-Pb zircon age of 610 ± 10.5 Ma (Oriolo et al., 2016a, b).

315 2.5.4. Maria Albina Shear Zone (MASZ)

316 The NE-SW trending “Fraile Muerto - Maria Albina Shear Zone” (MASZ) (Sánchez Bettucci et al., 2021;
317 Oriolo et al., 2016b) along the eastern border of the Pavas Block has been first considered the limit with
318 the DFB (e.g., Preciozzi et al., 1979). This shear zone shows a thrust-imbrication between the granitic
319 gneisses and the Las Tetras Complex supracrustal rocks (Oriolo et al., 2016a).

320 2.5.5. The Tupambaé Shear Zone

321 The Tupambaé Shear Zone (Sánchez Bettucci et al., 2021) shows granitic mylonites. Kinematic indicators
322 like foliation-fish and σ -type feldspar mantled porphyroclasts with tensional microfractures exhibit a
323 dextral shear (Oriolo et al., 2016b). The mylonites recorded a secondary paragenesis of fine-grained

324 biotite, epidote, and sericite, characterising retrogressive metamorphic conditions. σ_1 and σ_2 shears indicate
325 a dextral shearing under brittle conditions (Oriolo et al., 2016b).

326 2.5.6. Neoproterozoic metasediments and volcanic rocks

327 There are sedimentary successions in the NPT that constitute small, elongated, erosive relics formed by
328 syn-orogenic deposits of “molassic” nature (Fambrini et al., 2005; Masquelin, 2006). The Yerbal
329 formation (Gaucher, 2000; Blanco et al., 2009; Hueck et al., 2018) is another Ediacaran turbidite that
330 erosive superimposes the La China Complex. It shows a detrital zircon provenance indicating a
331 Cryogenian to Tonian maximum deposition age (Oyhantçabal et al., 2021). A deformation event separates
332 the Yerbal formation from the Barriga Negra formation. Ages between ca. 3.4 and 2.7 Ga are common in
333 detrital zircons from the conglomerates and sandstones of the Barriga Negra Formation (Blanco et al.,
334 2009; Peçoits et al., 2016; Oyhantçabal et al., 2021). The La China and Las Tetras complexes provided
335 large boulders of muscovite-rich orthogneiss, fuchsite-bearing quartzite, banded iron formation,
336 stromatolitic marbles and oligomictic meta-conglomerate to sustain the matrix-supported Ediacaran
337 conglomerate of the Barriga Negra Formation (Midot, 1984; Fambrini et al., 2005; Masquelin et al., 2017;
338 Núñez Demarco, 2019). The youngest detrital zircon age peak ($n \geq 3$) for the Barriga Negra formation is
339 581 ± 6 Ma (Blanco et al., 2009; Oyhantçabal et al., 2021).

340 3. METHODS

341 3.1. Geophysical data processing

342 Sander Geophysics Limited (SGL, Ottawa) performed and interpreted a partial airborne high-resolution
343 geophysical survey of magnetometry and gamma-ray spectrometry over Uruguay’s territory request of the
344 National Directorate of Mining and Geology, Uruguay (DINAMIGE). SGL carried out 196 data
345 acquisition flights. These flights operate between September 2014 and March 2015 (Bates et al., 2016).
346 The airborne survey products were: (i) the magnetic field anomaly map, (ii) the total count radiometric
347 map. The parameters for obtaining the airborne data were as follows: (i) drupe of 100 m above the digital
348 altitude surface, (ii) average flight speed: 130 knots (67 m/s), (iii) 400 m flight line spacing, (iv)
349 geomagnetic field parameters used for reduction to the Pole (RTP): inclination varies between -36.4° and $-$
350 41.8° and declination vary between -7.6° and -15.8° . Radiometric data have enough resolution for
351 lithological recognition. The imaging combines well with the existing geological information (Preciozzi et
352 al., 1985; Bossi et al., 2001). We made an accurate separation of rock units using airborne survey total
353 count radiometric (TCR) data and the horizontal (dx, dy) derivatives of the anomalous magnetic field map
354 reduced to the pole with an upward (1000 meters) continuation filter. This filtering accentuates the fields
355 due to different elevations’ sources, detecting the main deep-rooted NE-SW and N-S faults. The magnetic
356 and radiometric data aim to re-interpret the entire study area’s geological framework (the Nico Pérez
357 Terrane). The total count radiometry combines a shaded relief representation of the 12 meters ALOS-
358 Palsar digital elevation model (Advance Land Observing Satellite; UAF-NASA-JAXA, 2011). The

359 software Oasis-Montaj 8.5.0© (Geosoft Inc.) was used to plot geophysical data. Another achievement was
360 the DEM compilation and the total count radiometry map using the software QGIS (GNU).

361 **3.2. Analytical dating method**

362 We set up the isotopic data and zircon dating at the Geochronological Laboratory of the Geosciences
363 Institute from the University of São Paulo (Brazil). The LA-ICP-MS equipment locates at the CPGeo-
364 IGc/USP and has an excimer laser of ArF gas (193 nm) coupled to the Neptune™ High-Resolution Multi-
365 collector ICP-MS. The excimer laser used here provides a better regularity of abrasion, reducing the
366 fractionation between masses due to its high optical quality and source stability (Sato et al., 2009). The
367 ICP-MS analytical procedure was calibrated using the international standard zircon Temora-1 standard
368 zircon ($^{206}\text{Pb}/^{238}\text{U} = 0.06683$). Results are displayed in $^{206}\text{Pb}/^{238}\text{U}$ vs. $^{207}\text{Pb}/^{235}\text{U}$ Wetherill's Concordia
369 diagram and $^{206}\text{Pb}/^{238}\text{U}$ vs. $^{207}\text{Pb}/^{206}\text{Pb}$ Tera-Wasserburg's graph, using IsoplotR (Vermeersch, 2018).
370 Wetherill's Concordia diagrams served both to model magmatic protoliths' concordant age and the
371 systematic radiogenic lead loss due to subsequent geological processes. The zircons were ablated during
372 40 seconds in the 193 nm Excimer Laser Ablation System, at 7-6 Hz, 6mJ and full energy, obtaining spots
373 of ca. 25 μm (Helium: MFC1 = 0.300 L/min, MFC2 = 0.300 L/min, Argon: Aux.= 0.95 L/min, sample =
374 0.978 L/min).

375 **4. RESULTS**

376 **4.1. Geological interpretation using airborne radiometry**

377 Airborne radiometric maps can help to identify faults and geological contacts. The rationale for combining
378 total-count radiometry (TCR) with topography is to check structures already identified by
379 photointerpretation. The aim is to recognise the nature of the respective rocks on both sides of the
380 discontinuities, considering field information. The structural evidence provided by the combination of
381 geological maps and airborne geophysical data is multifaceted. An in-depth analysis of all the issues
382 cannot be done first-hand. We first documented the main faults to discuss kinematics. Therefore, we
383 checked structural settings for granites and identified tectonic structures. Finally, we build up an integrated
384 geological and geophysical map and profile, showing the most relevant features (Fig. 12).

385 **4.1.1 Main geological contacts and fault-kinematic analysis**

386 The Nico Pérez Terrane is complex because it encloses disrupted basement inliers that inherit many
387 structures from their Paleoproterozoic tectonic framework. The TCR map delimits two main sets of
388 radiometric values, (i) a high-intensity domain westward of the Cueva del Tigre fault (2) and the Sierra de
389 Sosa Shear Zone (c), and (ii) a low-intensity domain eastward of the said discontinuities (Fig. 3). Depleted
390 radiation areas appear in blue tones, while high radiation areas appear in fuchsia to pinkish-white shades.
391 The Pavas Block has the lowest radiometric values in the centre (< 800 cps; blue tones). These shallow
392 values represent an elongated N-S strip about 20-30 km wide. The "blue" area coincides with K-feldspar

393 depleted rocks. Only a few grey gneisses (metatonalites), amphibole-bearing granitic gneisses or diorites
394 could have a compatible composition in the field. The “blue” area is limited to the south by a mild yellow
395 space that matched with the exposure of metaconglomerates and quartzites, restricting it from the Polanco
396 carbonate area, in which radiometry values are low again. This carbonate area is cut to the east by a 170°
397 striking fault that controlled the Barriga Negra conglomerates and an exposure of muscovite orthogneisses
398 (high radiometry in both cases). Meanwhile, the Santa Lucia Batholith (SL) shows extremely high
399 radiometry values and sharp contacts.

400 Main faults display kinematic indicators based on the lithological identification at both sides of the
401 discontinuity. The low-radiometry elongated strip corresponding to grey gneisses and amphibolites is
402 crosscut by the Cueva del Tigre dextral strike-slip fault (2), giving two longitudinal halves that led to
403 interpret dextral shearing. This fault converges northwards to the María Albina fault (7) and the Caçapava
404 shear zone from Brazil, as already stated (Oyhantçabal et al., 2018). The eastern-lateral half of the Pavas
405 Block shows a narrow, stretched, and crenulated belt of quartzites, micaschists and marbles, partly
406 belonging to the Las Tetas Complex. The western half shows an exposition of granitic gneisses,
407 amphibolites and intrusive granitoids. Meanwhile, the northern part of the map constitutes an inverted
408 pull-apart full of low-grade metasediments. The pull-apart is between the sinistral María Albina (7) and
409 the Arbolito (6) faults, already known as the “Isla Patrulla - Yerbál region”. In the field, the succession
410 shows fold-interference patterns (Preciozzi et al., 1988a, b).

411 The TCR map (Fig. 3) highlights the presence of lineaments that are interpreted as conjugate faults
412 striking 035° and 170°, respectively (e.g., faults 1 and 4). The Cueva del Tigre (2) is a straight, brittle
413 fault. It overlaps the Sierra de Sosa ductile shear zone (c). The fault (2) is parallel to the Chamamé Fault
414 (4). A sigmoid fragment separated from the Illescas granite is among faults 2 and 4 in a strike-slip duplex
415 (Fig. 3). The radiometry of this fragment is the same as the leading granite. A dextral shear can be
416 interpreted for the movement of the fault (4). The Illescas Batholith shortened between faults (1) and (4)
417 and is regionally folded. An N-S regional extension (or a general E-W shortening) leads to a north
418 displacement of the Cerro Chato Block, a dextral movement of the Cueva del Tigre fault (2) and a sinistral
419 movement of the Cuchilla del Rosario fault (1). Recognising the lithologies on one side of the fault allows
420 evaluating the dislocation and establishing the shear sense. The Sierra de Sosa Shear Zone is interpreted as
421 a bent lineament, parallel to a sharp lithological boundary with the convexity to the East. It separates
422 layered gneisses and amphibolites, to the East, from alkali-feldspathic granitoids to the West. Although the
423 Pavas Block’s northern limit is likely the Tupambaé shear zone (Bates et al., 2016; Oriolo et al., 2016a),
424 the structure seems diffuse and full of granitic intrusions.

425 The Timote fault (3) strikes 035° and locates within the Piedra Alta Terrane (RPC) (Fig. 3). This fault
426 shows that the RPC margin must have suffered brittle deformation in its interior during the Brasiliano
427 orogenesis since it links to the Sarandí del Yí shear zone. Its conjugate fault is the Cuchilla del Rosario
428 fault (1), which is oriented 170°. The fault (1) appears as a late deformation reactivating the Sarandí del Yí

429 shear zone (6). Cataclastic breccias in dolomites of the Arroyo de la Pedrera Formation (Montana and
430 Sprechmann, 1993) accounts for the superficial character of this deformation.

431 *4.1.2 Radiometry pattern of supracrustal rocks*

432 In the Cerro Chato Block, there are small, elongated E-W strips, which contrast strongly with the high
433 TCR of surrounding K-feldspar-rich granites (e.g., Illescas granite) (Masquelin, 2006; Loureiro et al.,
434 2019). Their TCR is low (~1000 cps; light green tone) (Fig. 3). Some of them delineate folds or stay at the
435 corner between two conjugate faults. These bands represent erosion remnants of meta-sedimentary
436 sequences, like the Arroyo La Pedrera Formation. We identified at least seven strips of supracrustal rocks
437 that match field observations (Fig. 3). This pattern is mainly detected in the Cerro Chato Block.

438 The 070° dextral Tupambaé fault (5) cuts the contact between the Pablo Paez and the Pavas Block (Fig. 3).
439 Oriolo et al. (2016c) already discussed the later generation of this dextral conjugated fault. The radiometry
440 to the north of this Tupambaé fault (5) is equivalent to the Cerro Chato Block. The presence of
441 voluminous Neoproterozoic granites concordant with the gneissic layering (e.g., notably in the Pablo Paez
442 sub-region, e.g., Preciozzi et al., 1979) could explain such elevated radiometry (e.g., Cerrezuelo Granite,
443 CE, dated at ~619 Ma; Fort, 2020), but we cannot confirm that all the concordant granitoids will be
444 Neoproterozoic.

445 The supracrustal rocks of the Las Tetas Complex only crop out in the Pavas Block. Quartzites and
446 micaschists containing 600 Ma zircons appear in erosive relicts on the Cerro Chato Block. These
447 successions could represent an extensive sedimentary cover deposited (and deformed) at the final stages of
448 the Brasiliano orogenesis. The foliation that affected the different sequences of supracrustal rocks and
449 Paleoproterozoic granitoids appear refolded. The rocks show typical chevron and kink folds. The photo-
450 lineaments (in yellow lines; Fig. 3) represent the foliation directions. Otherwise, the structural
451 interpretation relies mainly on geological maps at the scale of 1:100,000 (Preciozzi et al., 1988a, b, 1989).

452 In summary, the TCR map shows discontinuous sectors having crenulated foliation with N-S axial-
453 directed folds. The kinks affecting the Las Tetas Complex represent a second tectonic event that overprints
454 this succession. Furthermore, these metasediments were already metamorphic before being affected by
455 this second generation folding. The quartzites have their own radiometric signature (the lowest TCR;
456 deep-blue tone). We can follow this quartzite layer along the eastern border of the La China Complex and
457 south of the Santa Lucia Batholith (SL). However, the Neoproterozoic Yermal formation cannot be easily
458 separated from the Las Tetas Complex at this scale in the TCR map (Fig. 3).

459 *4.1.3 Geological setting of Neoproterozoic granites*

460 Radiometric discrimination of granitoids is possible using different channels (eK, eTh, eU) but is beyond
461 the scope of this work. The shape and relationship with the background allow separating different
462 emplacement settings for granitoids. Using the TCR map, granitoids like the Zapicán diorite, it is

463 challenging to separate them from the La Chimba Complex because both are K-feldspar depleted. However,
464 in most cases, the granite emplacement setting provides a structural classification. Many granitic plutons
465 associate with displacements along the main shear zones. Some already dated plutons related to shear
466 zones help interpret the sense and period of the shearing. The lateral extrusion of Neoproterozoic late-
467 orogenic plutons (e.g., Guazunambí (GU) and Yermal (Y), i.e., 619 Ma; Fort, 2020) towards the south-
468 west of the sinistral Sierra Ballena Shear Zone (e) is evident (Fig. 3). In the same way, the Las Palmas
469 porphyritic granite (LP) emplaced in the Sierra de Sosa shear zone (c) likely follows a dextral lateral
470 extrusion.

471 Conversely, the older (633 Ma) and larger Santa Lucia granite (SL) (Bossi et al., 2001) locates in a
472 relatively low-strain location in the south of the Pavas Block. This is a relatively isotropic granite,
473 although slightly broken by brittle faults. Many conjugate 060° and 015° striking faults crosscut the Santa
474 Lucia granite (e.g., faults 8 and 9; Fig. 3). Santa Lucia granite's tectonic blocks overlap through shortening
475 in constriction. The entire body could be an elongated batholith, but now it is just a fragment "transported"
476 by the Pavas Block. Therefore, there is no connection with other granite's fragments in adjacent blocks.
477 Finally, some circumscribed circular post-tectonic granites appear in extensional settings (i.e., Tapes
478 Chico granite). The U-Pb zircon (SIMS) magmatic crystallisation age of the Tapes Chico Granite is 601 ± 5
479 Ma (Gaucher et al., 2019). Furthermore, this granite yields an $\epsilon_{\text{Hf}}(t) = -31$ and a TDM model age of
480 3088 Ma.

481 **4.2. Geological interpretation from the anomalous magnetic (dx1) derivative map**

482 The anomalous magnetic (dx1) first derivative map reduced to the pole (RTP) at 1000 meters elevation
483 (Fig. 4) reduced the high frequencies. Therefore, it provides information only about the first-order faults. It
484 also emphasises the existence of sharp boundaries between the different blocks of the NPT.

485 **4.2.1 Main geological limits of the Pavas Block**

486 Regarding magnetism, the anomalous magnetic (dx1) derivative RTP map at 1000 meters (Fig. 4) shows
487 minimal values in the Pavas Block, while it presents the highest values in the Cerro Chato Block. This
488 map represents the low frequencies. The low-magnetic pattern of the Pavas Block differs clearly from the
489 contiguous Cerro Chato and Villa Serrana blocks. This negative magnetic anomaly may be due to the
490 presence of altered mafic rocks depleted in magnetite. Low-magnetic susceptibility minerals like quartz
491 and feldspar in excess could be present. The upward continuation filter reducing the high frequencies
492 highlights the contrast of the limits, except in the south, where dykes cause high anomalies by
493 interference. In this map, the Sierra de Sosa shear zone resulted in a first-order magnetic boundary.

494 **4.2.2 Superimposed ferromagnetic dyke swarms**

495 Three WNW-ESE Mesozoic dyke swarms crosscut the mapped area. The southernmost swarm seems to be
496 connected by feeder dykes with the Cretaceous Valle Chico Complex (syenites and microsyenites)
497 (Preciozzi et al., 1985). These intrusive complexes represent geological landmarks here. The basement's

498 structural interpretation is difficult near these dyke swarms, mainly in the southernmost sector of the Pavas
499 Block. These dykes are high ferromagnetic dolerites that cause a wide anomaly, even at low frequency.
500 The elimination of high frequencies is not helpful for dyke discrimination if they are too close.
501 Consequently, the magnetic anomaly caused by many thin dykes will cause interference that can blur the
502 magnetic background.

503 *4.2.3. Main faults and horizontal lateral displacements*

504 While the Cueva del Tigre Fault (2) is better represented on the TCR map, the Chamamé Fault (4), which
505 is almost parallel to the former one (030°), stands out better on the dx1 anomalous magnetic map. The
506 resulting structure increases the fault visibility with a higher hierarchy and accuracy than those identified
507 by radiometry for the same faults. For example, the Valentines Complex shows rotated square boudins of
508 large dimensions, cut off by 070° and 140° striking faults. These blocks show contrasted high magnetic
509 values (Fig. 3) due to the high magnetic susceptibility of mafic gneisses and BIF found in these blocks.
510 Meanwhile, these boudins appear to be flanked to the south by the Cerro Valentín supracrustal belt (II),
511 which presents weak magnetic susceptibility.

512 *4.3. Zircon morphology, textures and U-Pb isotope data*

513 The selected zircons fall within the 70-300 μm grain size fraction. We carried out a comparative aspect
514 ratio. Zircons present different textural features when observed by cathodoluminescence (CL). These
515 microstructures allow us to advance in the knowledge of the metamorphic processes that affected zircons
516 from their origin. In general, there is a significant scattering of the Th/U ratios in almost all the samples
517 (Fig. 5). The bulk zircon histogram shows essentially two main accretion periods in the Archean and the
518 Paleoproterozoic (Fig. 8), although each age interval indicates much more complexity in terms of
519 geological events.

520 *4.3.1. Sample CNP13F*

521 This amphibole-bearing gneiss provides an almost regular zircon population (Annexe 1: Fig. 2a-d). Two
522 zircon types are identified, depending on the presence or absence of an inner core (Table II, Annexe 1):

523 (i) Majority (80%) of misty, pale brown, elongated, subhedral zircons with rounded ends. Their aspect
524 ratio varies from 3:1 to 5:1. Homogeneous, CL-dark zircons have blurred oscillatory zoning pattern
525 (OZP). The overgrowth is practically inexistent. The planar zoning is fading and broadening towards the
526 inner zones. Some features related to transgressive fronts, like void infilling (Fig. 6-1a) or CL-bright
527 internal patches (Fig. 6-1b). Basal prism sections are stubby (aspect ratio 2:1). A secondary
528 recrystallisation patch nucleates in the core-rim interface (Fig. 6-1c). Band replacement shows two
529 transgressive concordant bands, a CL-dark band, and a thin CL-bright trace element-rich seam.

530 (ii) Few zircons (~10%) show different oval-shaped inherited cores with sharp boundaries, and the
531 overgrowth is vast and unzoned. The core texture is contorted and surrounded by double-coated CL-dark
532 (outer) and CL-bright seams (Fig. 6-1d; Fig. 8a).

533 There are forty-four useful analyses (Table I, Annexe 1). Only three are in the rims. We plot them in a
 534 weighted mean age diagram (Fig. 9a) after filtering data with common lead (Pb^*) > 2 % and eliminating a
 535 few that are further away from the central age bar (Fig. 9b). Therefore, we reduce the MSWD of
 536 concordance and increase the probability $p(\chi^2)$. However, the method for calculating a central age only
 537 reveals that the ages decrease progressively, and there is no valid plateau (Fig. 9b). Then, we apply the
 538 “Discordia model-1” (Vermeesch, 2018) after filtering the data (Fig. 9c). We also used a Gaussian and
 539 Kernel density diagram (KDE) to discriminate age clusters (Fig. 9c, d). The Discordia line shows an upper
 540 intercept at 3270.8 ± 7 Ma and a lower intercept age at $ca. 1226 \pm 251$ Ma ($n=24$) (Fig. 9b). Some zircons
 541 are reverse-discordant. We relegate higher precision but managed to unravel inherited multiple magmatic
 542 sources (~ 3.33 and 3.26 Ga; MSWD=1.7). Finally, we applied the “Concordia model age” (Vermeesch,
 543 2018) to 11 selected zircons, with the lowest MSWD of concordance (0.03) and the highest probability
 544 $p(\chi^2) = 0.87$ (Fig. 9d). Spots located in unzoned overgrowths are scarce (Fig. 7-1d) but yield lower ages
 545 (~ 2.8 - 3.0 Ga; Fig. 9b). The KDE plot (Fig. 9b) shows multi-stage age clusters at 3.1, 3.25 and ~ 3.3 Ga
 546 ($n=24$). Its lower intercept is challenging to interpret without contrasting with other minerals’ dating with
 547 a lower closing temperature. The concordant age of 3246.8 ± 4.9 Ma (Fig. 9c) resulted from the plot of the
 548 same previous data ($n=11$), with an MSWD of 0.03 and a probability $p(\chi^2) = 0.87$.

549 4.3.2. Sample CNP77

550 This sample is extracted from a muscovite orthogneiss emplaced in a flat-lying shear zone (Annexe 1: Fig.
 551 2e-h). There is a mixture of five different zircon types in the sample size ($n=33$). All the grains are
 552 generally round and stubby. Most zircons show inherited cores and new growth rim. The round grains
 553 contain sealed fragments of fractured grains. The zircon types are the following:

554 (i) Round zircons showing an inner core with OZP (10%), surrounded by an outer body with CL in
 555 medium-grey shades and cloudy texture, the whole coated by planar non-luminescent seam and finally by
 556 planar CL-bright stitching (Fig. 6-3a).

557 (ii) Convolute recrystallisation surrounded by tight concordant non-luminescent recrystallisation seams
 558 (Fig. 6-3b).

559 (iii) Fractured zircon containing an inner unzoned core composed of bright and dark CL seams,
 560 surrounded by blurred OZP inherited outer magmatic centres, and fine external overgrowth (bright), and
 561 post-recrystallisation fracturing (20%) (Fig. 6-3c).

562 (iv) Blurred OZP attest to the magmatic inherited origin. A transgressive recrystallisation seam surrounds
 563 this sector zoning (Fig. 6-3d) (10%).

564 (v) Fractured grains are 35% of the sample; high luminescent material filled up the fractures. It witnesses
 565 metamict material loss.

566 There are 36 analysed spots, but the calculations of age only considered 13 spots. Three upper intercept
 567 $^{238}U/^{206}Pb$ ages have been determined: (i) 3353 ± 8.8 Ma (MSWD of concordance = 2.0) ($n = 4$), (ii) 3129
 568 ± 9.0 Ma (MSWD of concordance = 0.01) ($n = 4$), and (iii) 2976 ± 9.0 Ma (MSWD of concordance =
 569 0.43) ($n = 5$) (Fig. 9d; Table I, Annexe 1). These multiple ages probably reflect the mixing of zircons in

570 provenance from different Archean rocks. These concordances discriminate: (i) a Palaeoarchean (~3.5 Ga)
571 magmatic protolith (Fig. 6-3a), (ii) a Mesoarchean (~3.1 Ga) population (Fig. 6-3d), and (iii) a
572 Neoarchean (~2.8-2.7 Ga) post-peak zircon growth (Fig. 6-3d). The MSWD of concordance is far from 1
573 except for the oldest group (above 3.3 Ga). However, there are too few samples to be able to conclude.
574 The kernel density plot (KDE) and histogram (n = 27) show a tendency towards the separation of these
575 three groups (Fig. 9d).

576 4.3.4. Sample Mi21

577 This Hbl-bearing tonalitic orthogneiss (Annexe 1: Fig. 3a-f) gives subhedral to round and mostly fractured
578 zircons. Their aspect ratio shows a normal distribution (maximum at 2:1). The texture shows a separation
579 between the OZP of the inherited grain and multiple recrystallisation fronts. Fronts go from outside to
580 overlap themselves inside and partially. The overgrowth leads to sector zoning (planar, radial, fir-tree
581 zoning). There are two zircon kinds:

582 (i) Containing outer (2) and inner (1) cores; OZP is widespread, and secondary recrystallisation obliterated
583 both the rims and bodies (90% of zircons). OZP are relicts of inherited magmatic zircon. Older and darker
584 CL inner cores (1) contain visible OZP (Fig. 6-4a). Both centres (1 and 2) are affected by transgressive
585 recrystallisation fronts. The main OZP's preservation (Core 2) depends on the advance of multiple
586 recrystallisation fronts (Fig. 7c), except for some fading/broadening of specific bands (Fig. 6-4b). An
587 external transgressive front is close to the boundary of core 2 (Fig. 6-4c).

588 (ii) Complex inner cores (10%) with patchy zoning or convolute pattern, surrounded by bright CL rim
589 (local recrystallisation). CL-dark bands come from secondary dissolution/reprecipitation (Fig. 6-4d; Fig.
590 7c).

591 The Mi21 sample provides 36 single spot analyses. Eight zircons come from recrystallisation rims.
592 Typical from these Archean zircons, Th/U values are extremely dispersed (Fig. 5). Two spots yielded a
593 common Pb in excess (>5%), but we assume that many values indicating zero are abnormally low. After
594 making a wide selection of zircons according to the content of common Pb, we determined a concordant
595 age of 3137.5 ± 4.4 Ma (n=6), with an MSWD of concordance about ca. 0.0052 and a probability $p(\chi^2) =$
596 0.94 (Fig 9e). We tried the nominal Pb correction algorithm provided by the IsoplotR program
597 (Vermeesch, 2018) to perform this probability. Then, we conducted another test, applying the Discordia
598 model-1 for overdispersion in the IsoplotR (Fig. 9f). Sixteen spots in these grains define a Pb-loss
599 regression, which intercepts the Concordia at 2986 ± 5 Ma (upper intercept) and 1804 ± 17 Ma (lower
600 intercept) (MSWD = 5). The weighted mean diagram shows the age dispersion corresponding to the lower
601 intercept (MSWD = 22.5) (Fig. 9f).

602 4.3.5. Sample Mi30

603 These zircons come from the mesosome of the biotite-bearing migmatitic orthogneiss (Annexe 1: Fig. 4a-
604 f). They are subhedral to round, and the aspect ratio is 2:1. Many of them show fractures and rough

605 borders. Saturated grains provide some cores. They conduct an extreme development of the sector zoning
606 pattern during recrystallisation, but we can interpret the remnants of OZP (Fig. 6-5c). The zircon types are:
607 (i). Zircons replaced and recrystallised by sector zoning (Fig. 6-5a, 5b). Planar or angled sector zoning of
608 the type “fir-tree” is typical (Fig. 6-5b; Fig. 7d). This feature affected almost the entire zircon, except CL-
609 bright transgressive fronts crosscutting the rims. The same zoning pattern recrystallises the cores, but CL-
610 darker.

611 (ii) Zircons with broadened bands issued from OZP (except the CL-dark centre) but surrounded by sector
612 zoning recrystallisation replaces the original bands. Transgressive fronts are conspicuous and achieve the
613 replacement evolution (Fig. 6-5c).

614 (iii) Zircons enclosing inherited patchy cores, surrounded by CL-dark seam and sector zoning rim (Fig. 6-
615 5d).

616 The Th/U values follow a perfect regression line (Fig. 5). There are 31 over 36 useful analyses (Table I,
617 Annexe 1); nine are in the rim. One zircon (Mi30-2.1) has two spots in one core (Fig. 6-5a). The grain
618 selection criteria depended on the low common lead contents. The Concordia model plot the assignment (n
619 = 10). In this plot, a common lead correction was done according to the Stacey-Kramers function provided
620 by the IsoplotR program (Stacey and Kramers, 1975). We obtained a bimodal data set. The Wederhill
621 diagram shows a concordant age of 3074 ± 7 Ma (MSWD=1.9) for the oldest data set (Fig. 10a). We
622 performed a second test through the Tera-Wasserburg diagram for the younger data set ($n=31$) without
623 common Pb correction (Fig. 10b) that yields a concordant age of 1839.6 ± 2.0 Ma (MSWD = 0.71). A
624 significant over-dispersion of likelihood results displays along with the Concordia (~200 Ma). A Discordia
625 chord shows a connection between both data sets. The younger one is interpreted as the metamorphic
626 replacement/crystallisation age.

627 4.3.3. sample Mi14

628 This zircon sample was extracted from a biotite-bearing recrystallised granitoid (Annexe 1: Fig. 5a). The
629 grains are euhedral, fractured, roughly, and their aspect ratio is 2:1 on average. Many zircons show
630 annealing (core and rim). The annealing produced a multifaceted mosaic texture. Most zircons have an
631 extensive, unzoned overgrowth but generally preserve few oscillatory zoning traces. Annealed zircons
632 have a smooth separation between core and rim, which is interpreted as a chemical recrystallisation front.
633 The annealed cores preserved some relic non-luminescent inclusions. Besides, some patches grew along
634 with different interfaces of zoning. Zircon kinds are the following:

635 (i) Dark-CL cores with non-luminescent inner parts, enriched in trace elements, seems a relic of the recoil
636 after the annealing. They probably contain porous metamict material (Figs. 6-3a, b) or remnants that were
637 almost wholly solved (Fig. 6-3c, d). The annealing affected the lattice of many cores (multifaceted
638 appearance). The rim is bright-CL.

639 (ii) Bright-CL cores, depleted in trace elements, also retain some relic of the recoil after the annealing
640 (Fig. 6-3c). The annealing preserves the euhedral crystal, which could be evidence of magmatic protolith
641 (Fig. 7e). The polygonal aspect of the core; conversely, the rim is dark-CL.

642 (iii) Hissile zircons without cores. Some centres are CL-dark but small and fuzzy. Some sector zoned
643 broadened bands replaced the original OZP in the body (Fig. 6-3d). There is also some CL-bright
644 transgressive front in the periphery.

645 We retrieve 36 useful analyses. Th/U show wide dispersed values and total Pb content (%) is high. The
646 plot shows two different populations (Fig. 10c). They correspond to (i) Archean and (ii) Paleoproterozoic
647 zircons. The selected zircons include inherited Archean cores, filtered by low common Pb. We plot two
648 isochrons (IsoplotR - Discordia model-1) (Fig. 10d). The upper intercept yields an age of 2973 ± 15 Ma and
649 the lower intercept age of 1887 ± 28 Ma (MSWD = 3.2). The first is interpreted as the inherited
650 metamorphic/magmatic age of the protolith, whereas the second is considered as the crystallisation age of
651 the new melt. A secondary Pb-loss Discordia regression line yields 1917 ± 12.6 Ma (upper intercept) and
652 1037 ± 146 Ma (lower intercept) ages (MSWD = 0.58) that is interpreted as Pb-loss resetting due to a
653 second tectonic event. The latter lower intercept is not well constrained (Fig. 10e). A weighted mean age
654 plot shows a drop at ~ 1.8 Ga.

655 4.3.6. Sample Mi19B

656 This sample comes from a mylonite (K-feldspar granite) sharing the layering with a biotite/tourmaline
657 mica-schist (Annexe 1: Fig. 5b-d). Zircons are dominantly subhedral, multifaceted with a variable aspect
658 ratio (2:1 to 3:1). Also, rounded oval-shaped zircons are present. They are translucent and show weakly-
659 defined oscillatory zoning. Most cores are sector zoned and CL-bright, but the recrystallised oscillatory
660 bands in the centre are broadening (Fig. 6-6a). Radiation damage produced radial cracks, which usually
661 cut the rim overgrowth (Fig. 6-6b; Fig. 7f). Some zircons contain CL-dark, round inner cores. The rims
662 show relics of oscillatory zoning (Fig. 6-6c, d). Transgressive recrystallisation fronts bulge towards the
663 centre. Unzoned patches also appear between the centre and rim (Fig. 7f). The inner core often shows non-
664 luminescent bands surrounded by CL-bright seams. Non-luminescent material locates along with fractures.
665 Th/U is comparatively less dispersed than in other samples and close to magmatic values (Fig. 5). The
666 zircons of this Paleoproterozoic granite do not have any previous inheritance (e.g., Archean). This
667 sample's Eleven spots gave a poorly constrained Pb-loss regression line (Discordia Model-1) showing
668 highly discordant grains. The isochrone cuts the Concordia at 1987 ± 3 Ma (upper intercept) and at 783 ± 18
669 Ma (lower intercept) (MSWD = 2.8) (Fig. 10f). An attached Tera-Wasserburg plot using the Concordia
670 model without any corrections shows the natural dispersion of data (n=16) in the upper intercept giving an
671 age value of 1999.6 ± 3.1 Ma (Fig. 10f). Significantly few 2SE ellipses fall on the Concordia, and the
672 MSWD is higher (8.1). The older age is interpreted as the magmatic crystallisation age. The lower age at
673 783 ± 18 Ma could be an isotopic disturbance during Neoproterozoic recycling.

675 **5.1. Interpretation of U-Pb zircon ages and textures**676 *5.1.1. Advances and limitations in the interpretation of U-Pb ages*

677 The relative excess of Pb in most zircons of the La China Complex can be attributed to Pb gain rather than
678 to U and Th loss. Meanwhile, changes in the Pb/U ratio and Pb isotopic composition correlated directly
679 with Pb concentration (e.g., Williams et al., 1984). Pb-gain seems to be a common situation in Archean
680 granitoids. The youngest ~2.7-2.8 Ga zircon ages analysed by SHRIMP in the La China Complex
681 (“sample-1”; Table III, Annexe 1) were considered as formed during a metamorphic event (Hartmann et
682 al., 2001). Their oldest ~3.4 Ga zircon age was interpreted by these authors as the magmatic crystallisation
683 age. However, the reliance between $^{238}\text{U}/^{206}\text{Pb}$ and $^{207}\text{Pb}/^{206}\text{Pb}$ is between 102% and 107% in many
684 analysed grains. When applying the Discordia model-2 (Vermeesch, 2018), zircons distribute along with a
685 Pb-loss isochron. The isochron has an upper intercept at 3380 ± 27 Ma and a lower intercept at 2422 ± 100
686 Ma (n=12). Our zircon samples CNP13F and CNP77 (Fig. 9a-d; Table I, Annexe 1) come from the same
687 unit a few kilometres from “sample-1”. The elevated common Pb makes the concordant age complicated.
688 Archean zircons from igneous protolith likely preserved multi-stage magmatic ages almost unmodified
689 even after being affected by replacement or overgrowth. Zircon textures in the sample CNP13F are typical
690 of high-grade metamorphic rocks (Hoskin and Black, 2000). They consist of a homogeneous population of
691 recrystallised zircons. These zircons almost completely lose their regular oscillatory pattern (Pidgeon et
692 al., 1998; Vavra et al., 1999; Corfu et al., 2003). The fading and broadening of ancient oscillatory zoning
693 are due to recrystallisation/replacement processes (Pidgeon, 1992; Hoskin and Black, 2000). Some grains
694 indicate solid-state recrystallisation within a sustainable closed system (Fig. 7-1b, d) (Schaltegger et al.,
695 1999; Rubatto, 2017). Secondary recrystallisation fronts drive grain boundary migration and defect
696 diffusion to recover trace element accumulation at high-strain lattice settings (Geisler et al., 2007). Trace
697 element partitioning between depleted vs. enriched sectors also provides compelling evidence for solid-
698 state replacement (Pidgeon, 1992; Hoskin and Schaltegger, 2003). Our recrystallised zircons may
699 represent multiple Archean tectono-thermal events. These zircons still have the problem of their protracted
700 residence in conditions above 600°C, which probably determines the Pb-loss due to slow diffusion over at
701 least 200 Ma. A protracted residence above 600-650°C is needed to reach the conditions in which
702 metamict zircon is still recovered (Mezger and Krogstad, 1997). This evolution determines a sequential
703 radiogenic Pb-loss due to slow diffusion over time rather than an excess temperature. The apparent
704 “concordance” in the sample CNP13F may be due to the continuous annealing process above the
705 recovering temperature (Mezger and Krogstad, 1997). Considering zircon textures, we assume that the
706 magmatic age exceeded ~3.1 Ga. The Concordia model yields an age of 3247 ± 5 Ma (MSWD of
707 concordance = 0.03; n=11) (Fig. 9c). The resulting diagram indicates an over-dispersion (spanned from
708 3300 to 3100 Ma). The excess in common Pb and scattering of Th/U ratios suggest that the U-contents
709 obliterated slowly but deeply during this recycling. The “nearly concordant age” interpretation must

710 consider the youngest zircons as shown to interpret a new zircon growth (Fig. 7-1d). The low-U contents
711 imply that further Pb-loss by recycling will be progressively less effective through time as the U and Th
712 reservoir would be depleted. These scattered ages likely represent the recrystallisation from protracted and
713 continuous magmatic sources >3.1 Ga (Fig. 8c) rather than the result of multiple events.

714 In summary, the La China Complex contains contrasted hornblende-bearing vs. muscovite-bearing
715 orthogneisses. Their protoliths crystallised up to 3.1 Ga. They were further affected by Neoproterozoic
716 tectono-thermal events (2.7-2.8 Ga). Samples taken from the block's centre did not record any sign of
717 post-Archean recycling. However, the Ar/Ar method shows cooling ages reporting Neoproterozoic
718 reactivation (Oriolo et al., 2016a, b). Otherwise, Pb-gain in zircons could be related to hydrothermal-
719 metasomatic processes typical from the Archean (e.g., Frei et al., 2002). Our samples CNP13F and CNP77
720 contain three sets of U-Pb ages but slightly different time intervals scattered between ~3.3 Ga and 2.6 Ga
721 (Fig. 9b, c, d; Fig. 11). Still, the CNP77 muscovite gneiss could represent an injected concordant
722 pegmatite emplaced within the flat-lying foliation of a biotite-bearing gneiss in an overthrust (Annexe I:
723 Fig. 2e-h).

724 *5.1.2. Episodic magmatic flare-ups during the Archean or chaotic inheritance?*

725 A comparative study based on the Kernel density estimation (KDE) between Archean samples (Sample-1;
726 CNP13F; CNP77; Mi21) shows that older clusters are separated by ca. 30-50 Ma, but they are not the
727 same in all the samples (Fig. 11). The bulk U/Pb zircon ages suggest an optimum bandwidth of 25-30 Ma
728 for many key features, which yields approximately 40 peaks with confidence levels of $c \geq 0.9$ (Condie and
729 Aster, 2010). According to Hartmann et al. (2001), Sample-1 shows three peaks: (i) older than 3.30 Ga,
730 (ii) 3.00 - 3.25 Ga, and (iii) 2.65 - 2.95 Ga (Fig. 11). CNP13F shows homogeneously recrystallised zircon
731 textures, with blurring magmatic features (Fig. 6.1a-d) and three main age clusters: (i) 3.1-3.4 Ga, (ii)
732 2.85-2.9 Ga, and (iii) 2.5-2.65 Ga (Fig. 11). However, the concordant data are mostly concentrated up to
733 3.1 Ga (Fig. 9b, c, d). Meanwhile, these zircons show high dispersion of Th/U ratios (Fig. 5) and low U
734 contents (<50 ppm) (Table I, Annexe 1). Hartmann et al. (2001) interpreted the rim ages as the M₁
735 amphibolite facies metamorphism period. La China Complex's samples have in common a scarce record
736 of ca. 2.5-2.9 Ga metamorphic events, but further statistics will require to improve accuracy. The
737 traditionally made inference that zircon U-Pb ages date the intrusion or emplacement of magmatic rocks is
738 difficult to sustain here (e.g., Schaltegger and Davies, 2017). The statistically dominant U-Pb zircon age
739 clusters may reflect the age of source rocks rather than the igneous crystallisation age (e.g., Crowley,
740 2003). Indeed, in such protracted residence (3.4 to 3.1 Ga), source rocks mainly represent preceding TTG
741 granitoids, which represent ~50% recycled primitive oceanic upper plate, including recycled sedimentary
742 rocks (Frei et al., 2002; Ducea et al., 2015). On the other hand, the magmatic crystallisation interpretation
743 does not forget discriminating between the different multi-episodic pulses of magma accretion separated
744 by lull periods (Ducea et al., 2015). If Archean magmatic arcs were formed in the same way as
745 Phanerozoic's, therefore, Archean magma accretion also characterises as punctuated equilibrium, whereby
746 long periods of quiescence are interrupted periodically by short events of high-volume magmatism called

747 flare-ups (Ducea et al., 2007). This pulsatile behaviour impacts deeply the statistics about the U-Pb
748 zircon ages. The process also affects that of detrital provenance that depends on the same granite sources
749 (e.g., De Silva et al., 2015). The repetition of “nearly concordant” zircon ages in La China Complex could
750 not be explained just by inheritance. On the other hand, there is no record of a single magmatic event that
751 lasts through 300 Ma during the same orogenic event. Paleo-Archean metamorphosed zircons, which show
752 that sparse distribution of “nearly concordant” ages, deserve to be cautiously discussed. Therefore,
753 different generations of multi-stage magmatic zircons could represent an Archean equivalent of the
754 Phanerozoic magmatic flare-ups during protracted subduction (Ducea et al., 2015).

755 *5.1.3. What information does the U-Pb system offer about the thrusting age?*

756 The presence of an overthrust carrying muscovite orthogneisses in the middle of the La China Complex,
757 being part of the Sierra de Sosa Transcurrent System (Campal and Schipilov, 1999), was first dated by the
758 K/Ar method, which yields an age of ca. 1253 ± 32 Ma, reported for “synkinematic muscovite” (Bossi et
759 al., 2001). Then, the sample ZAP20 (Gaucher et al. 2011; Table III, Annexe 1) yield a discordant upper
760 intercept age of 3096 ± 45 Ma and a lower intercept of 1252 ± 900 (MSWD = 5.4) (n=4/12), which
761 conveniently match the K/Ar result. The upper intercept age (~3.1 Ga) was interpreted as the main
762 metamorphic event, but 90% of analyses are in the cores. Our sample CNP77 comes from the overthrust
763 itself. Most of their zircons are rounded and fractured. They are often composed of core and mantle, sector
764 zoning and transgressive recrystallisation fronts (Fig. 7b). These zircons are usually half of the broken
765 prismatic zircons due to grain size reduction by strain (e.g., Corfu et al., 2003). Few zircons that represent
766 the “M₂ metamorphism” yield ~2.6-2.8 Ga (Fig. 9d; Fig. 11). These cracks did not form by radiation
767 damage but also by deformation (Wayne and Sinha, 1988). Indeed, radiation-damaged parts are weak and
768 more likely to nucleate tectonic fractures (Lee and Tromp, 1995). On the other hand, we found a minor
769 assemblage of grains having nebulous zoning or flowing structure, likely formed at granulite-facies
770 conditions (Pidgeon et al., 2000). These zircons yield ages close to ~3.12-3.16 Ga. Otherwise, the oldest
771 zircons yielded ~3.7 Ga, and the youngest ~964 Ma. This age population matches with the overall
772 Archean inherited zircons. Therefore, flat-lying mylonites in sample CNP77 occurred after the Archean.
773 The presence of a ca. 1.0 Ga zircon suggests that the overthrust could be post-Archean but does not
774 produce any measurable overgrowth.

775 *5.1.4. The Orosirian melting and metamorphic overprint*

776 Except for the Archean core, all the peripheral samples from the La China Complex (i.e., Mi21, Mi30,
777 Mi14, and Mi19b) underwent advanced recycling with metamorphism and anatexis in the Orosirian Period
778 (ca. 2.0-1.8 Ga). Despite the penetrative distribution of this recycling, zircons rarely recorded
779 Neoproterozoic ages. Unlike the Cerro Chato and Rivera blocks, in which Rhyacian magmatism (ca. 2.1
780 Ga) and granulitic metamorphism (ca. 2.08 Ga) are widespread (Tickyj et al., 2004; Oyhantçabal et al.,
781 2012; Girelli et al., 2018), these events are not recorded in the Pavas Block. An age lull characterises the
782 Siderian to Rhyacian period at this setting (Fig. 8). In the Orosirian, the South American Platform evolves

783 in many ways, with important accretionary and collisional orogenic events (Brito Neves, 2011). In the
784 Pavas Block, the recycling record of the Orosirian metamorphic event is uneven depending on the site.
785 The sample Mi21 is a hornblende-bearing metatonalite with magmatic crystallisation at 2986 ± 5 Ma (Fig.
786 9f; Annexe 1: Fig. 3a-f). The lower intercept at 1804 ± 17 Ma represents a Pb-loss due to amphibolite facies
787 metamorphism (Fig. 9f). Their zircons (Fig. 6.4a-d) shows the best-preserved inherited magmatic textures
788 from a Neo-Archean intrusive granitoid recrystallised by the ~ 1.8 -1.9 Ga metamorphism (Fig. 9e-f). The
789 oscillatory zoning pattern slightly changed during metamorphism, as indicated by bands' broadening (e.g.,
790 Pidgeon et al., 1992). The successive transgressive fronts also preserved the inherited magmatic textures
791 (Fig. 7c).

792 The sample Mi30 is a layered migmatite that shows complex-textured zircons (Annexe 1: Fig. 4a-f). In
793 this sample, the inherited oscillatory pattern is rare (Fig. 6-5c). The Orosirian migmatites reveal a higher
794 concentration of 1.8-1.9 Ga concordant zircon ages (e.g., Mi30; Fig. 10a). The Th/U regression line (Fig.
795 5) suggests that the lower intercept connects with the ~ 1.8 Ga leucosome as a fractionated crystallisation
796 process. However, sector zoning (e.g., "fir tree"; Fig. 8d) or an absence of zoning mostly overlap inherited
797 zircon core's textures. Secondary recrystallisation fronts can mask the new texture partially (Fig. 6-5c).
798 These zircons display bimodal concordant age clusters, one Neoarchean and the other Orosirian (Fig. 10a,
799 b). The 'concordance' model reveals a higher concentration of Orosirian ages at 1839.6 ± 2 Ma ($n = 21/31$)
800 when applying the common Pb correction algorithms (Vermeesch, 2018). This age is interpreted as melt
801 crystallisation. Although the host rock is not a granulite, "fir tree" zoning may characterise some zircons
802 that underwent granulite-facies conditions (Pidgeon et al., 2000; Corfu et al., 2003). The Archean
803 concordant age data cluster represent its granitic protolith ($\sim 3074 \pm 7$ Ma; $n = 10/31$) (Fig. 10a). This rock
804 was subsequently affected by an Orosirian tectono-thermal event, producing little or no overgrowth. These
805 ratios grown in the presence of partial melt may approach that of igneous zircon due to the monazite
806 anatexis breakdown (Montel, 1993; Kohn and Kelly, 2018). Monazite can destabilise in the melt to form
807 allanite (Lee and Bastron, 1967). Indeed, the allanite is ubiquitous in the neosome of sample Mi30
808 (Annexe 1: Fig. 4e).

809 Another sample (Mi14) represents the grey orthogneisses of the La China Complex (Annexe 1: Fig. 6d-h).
810 In this sample, the high-grade metamorphism seems obliterating by low temperature hydrothermalism.
811 Meanwhile, multi-episodic Pb-loss has been recorded in zircons. Sample Mi14 displays an inherited zircon
812 core population yielding an upper intercept age of 2973 ± 15 Ma and a lower intercept of 1887 ± 28 Ma
813 (Fig. 10d). The lower intercept age represents the overgrowths before the second metamorphic event.
814 Then, a Discordia line can be plotted between the upper intercept at 1917 ± 13 Ma and a lower intercept of
815 1037 ± 146 Ma (Fig. 10e). However, the real interest of this sample is in its texture. Although there are
816 different zircon textures on it, one texture family shows almost complete annealing of cores and rims (Fig.
817 6.3b, c). This sample is unlikely to come from a granitoid, as evidenced by the unzoned cores, devoid of
818 the oscillatory pattern (Fig. 6-3b, c; Fig. 7e). The oscillatory pattern also lacks in the rims. The polygonal
819 texture indicates partial to complete annealing on these zircons (Fig. 8e). Structural annealing is a common
820 feature in granulitic zircon (Schaltegger et al., 1999; Corfu et al., 2003). Mechanisms proposed as being

821 responsible for redistribution of Pb are the annealing of radiation damage (e.g., Nasdala et al. 2002), fluid
822 alteration (e.g., Geisler et al. 2002), crystal plastic deformation (e.g., Reddy et al. 2006), and annealing
823 due to crystal lattice strain (e.g., Schaltegger et al. 1999). The annealing process represents a
824 reorganisation of the zircon lattice in the solid-state. It involves the reestablishment of Zr-O bonds,
825 disrupted by the recoil of the radiation decay (Schaltegger et al., 1999). The driving force may be the
826 differential lattice strain between low-U and high-U growth zones. Radiation damage's annealing is
827 common in natural zircons. Therefore, the recrystallisation process must be occurred by the conjunction
828 between a crystalline recovery of an old, damaged zircon and the overall thermodynamics of
829 metamorphism (Nasdala et al., 2001). In contrast to recrystallisation/replacement, annealing recovery is
830 not necessarily connected with Pb-loss. Hydrothermal fluids may assist post-metamict annealing but do
831 not necessarily reflect a dissolution - reprecipitation process (Geisler et al., 2003). In the case of sample
832 Mi14, we interpret the intermediate age (1917 ± 13 Ma) as the partial melt crystallisation (Fig. 10e).
833 Meanwhile, the lower intercept age reflects a second Pb-loss due to a second tectono-thermal event of ca.
834 1.1-1.3 Ga. The fluid-enhanced annealing of the amorphous parts in metamict zircons is well-known from
835 hydrothermal alteration experiments (Geisler et al., 2003). Radiation-damaged recovery is a coupled
836 diffusion-reaction and recrystallisation - controlled process (Geisler et al., 2007). In natural zircon
837 submitted to experimental annealing above 830 °C, the recovery occurs in a two-stage process from
838 amorphous material to form new zircon. This process leads to different microstructures, depending on the
839 initial amount of radiation damage. At higher experimental temperature (above 1320°C), the assemblage
840 transforms into a polygonal texture of small zircon grains (Ginster et al., 2019). In summary, the
841 Orosirian tectono-thermal event is a high-grade metamorphism with different degrees of partial melting
842 and metamorphic recrystallisation on zircons, sometimes coupled with lattice annealing, in the southern
843 and western parts of the Pavas Block.

844

845 **5.2. Extension of the Pavas Block**

846 *5.2.1. What defines the borders of the Pavas Block?*

847 The extension of the Pavas Block does not match that of the exposed Archean rocks. As Mallmann et al.
848 (2007) already stated, “*only a very restricted set of rocks have Archean crystallisation ages.*” These rocks
849 have tonalitic protoliths, crystallised from a mantle source between 3.1 Ga to 3.4 Ga. The Sm-Nd TDM
850 model ages in an amphibolite suggest that recycling could be Paleoproterozoic (Mallmann et al., 2007).

851 The southern border of the Pavas Block is related to an earlier structure connected with the Sarandí del Yí
852 shear zone. This region preserves a flat-lying shear zone remain of almost twenty kilometres wide and
853 thirty kilometres long in the region called Espuelitas (Fig. 12). Supracrustal rocks are involved as roof-
854 pendants. It could be a fragment of an abandoned NW-SE striking lateral ramp, which cannot equate with
855 the actual Sarandí del Yí Shear Zone. This shear zone clearly records a strike-slip movement as judging by
856 the strong parallelism of lineations and upright folds (Masquelin et al., 2017). The sample Mi19B was

857 connected within one of those folds of the mylonitic foliation. The K-feldspar granite (mylonite) does not
858 show any Archean heritage (Fig. 10f). It yields an upper intercept age of 2000 ± 3 Ga (MSWD=8),
859 interpreted as magmatic crystallisation. Zircon grains are translucent, U-rich and metamict (α -decay
860 damage cracks). The K-feldspar granite was mostly deformed during the Neoproterozoic (783 ± 18 Ma)
861 under lower amphibolite facies conditions, together with the host rock, a tourmaline-biotite micaschist
862 (Annexe 1: Fig. 5b-d). Another SE-structure near the southern contact is the Mesoproterozoic schist belt,
863 named the Tapes Complex (Gaucher et al., 2019), which results in a natural frontier between the Villa
864 Serrana and Pavas blocks. In summary, all this evidence suggests that the Pavas Block's southern
865 boundary is flanked by abundant Orosirian magmatism. Also, the Espuelitas flat-lying strike-slip shear
866 zone acts as a transitional basement that dislocated during the Cryogenian.

867 5.2.2. How far the Las Tetas Complex does extend?

868 Another question concerning the Pavas Block's limits is how far the exposure of the Las Tetas Complex
869 extends (Hartmann et al., 2001). The field information indicates that all the block has a "basement-cover"
870 structure like any fold-thrust belt (Fig. 13). This mylonite deformed by late folds affecting the Las Tetas
871 Complex and reactivating the basal unconformities behind the La China Complex. Both units share the
872 same low angle mylonitic foliation, verging towards the south.

873 The Las Tetas Complex's regional extent is continuous for more than a hundred kilometres from the north
874 until Minas's town in the south (Gaucher et al., 2014). Fuchsite-bearing quartzites and metaconglomerates
875 may reach hundreds of meters in thickness (Hartmann et al., 2001). The thrust-stacking produced
876 muscovite-bearing S granitoids with the foliation parallel to the thrust planes within the La China complex
877 (Hartmann et al., 2001). The deformation events that made the overthrust are in amphibolite facies
878 metamorphism. Later upright folds produced the bending of sub-horizontal thrust planes. Muscovite-
879 bearing S-granites crosscut the Las Tetas Complex. The Parque Salus oligomictic metaconglomerate
880 (Midot, 1984; Masquelin, 2006) can be linked with the Las Tetas Complex and the Campanero and Aguila
881 hills fuchsite-bearing quartzites and BIF. Black quartzites, amphibolites, marbles, BIF, tourmaline-biotite
882 schists, and fuchsite quartzites associated with the Villalba Hill Formation (i.e., Bossi and Gaucher, 2014)
883 also represent an equivalent. Finally, the carbonate-quartzite association in the Polanco region describe an
884 extensive carbonate succession as the basement of the Ediacaran Barriga Negra Formation (Masquelin et
885 al., 2017; Núñez Demarco, 2019). We believe that all these rocks may represent equivalents of the Las
886 Tetas Complex. Fuchsite-bearing quartzites and metaconglomerates associated with BIF likely represent
887 lithotypes from Paleoproterozoic marine sequences submitted to pre-Neoproterozoic hydrothermal
888 alteration. The Siderian global climate change at ~ 2.45 Ga, known as the "Great Oxidation Event" (GOE;
889 Bekker et al., 2004; Konhauser et al., 2011), maybe the cause of chromium solubility and alteration of the
890 Las Tetas Complex. The marked differences in metamorphic grade between the Las Tetas Complex and
891 the Neoproterozoic cover suggest that chromium dispersal was principally Orosirian and syn-
892 metamorphic. Most of the stromatolite-rich dolostones found in different settings between the centre and
893 the extreme south (near the Minas city) (e.g., Gaucher et al., 2006) are likely related to the Las Tetas

894 Complex. Erosive unconformities found in this region between the Ediacaran cover above the medium-
895 grade metamorphic Las Tetas Complex (e.g., Masquelin et al., 2017) are not affected by the chromium
896 hydrothermalism.

897 5.2.3. Contribution concerning the “exotic” Pavas Block

898 The NPT proved to be allochthonous concerning the Río de la Plata Craton (Oriolo et al., 2015;
899 Oyhantçabal et al., 2018). However, primary accretion’s period preceding the NPT amalgamation is
900 unknown. On the one hand, different inherited heterogeneities must be analysed, like the presence of a
901 disrupted piece of a Neoproterozoic batholith (i.e., Santa Lucia granite; SL) placed transversely in the
902 south of Pavas Block. This granite does not match with any other of the same age (ca. 630 Ma), from the
903 neighbouring blocks. This “exotic” K-feldspar granite crystallised in a low-strain environment,
904 highlighting the complexity of the Neoproterozoic amalgamation in the NPT. On the other hand, the
905 inherited metamorphic grade and the restrained setting of the Las Tetas Complex compared with those of
906 Neoproterozoic units led to questions about the “suspected” provenance of the Pavas Block. This block
907 could be first a Paleoproterozoic terrane displaced during the Rhyacian accretion within the Columbia
908 Paleo-continent, like many others around the São Francisco Craton (e.g., Ávila et al., 2010; Martins-
909 Ferreira et al., 2020) before becoming “Brasiliano”.

910 One of the most accepted ideas concerning the secondary intracontinental amalgamation is that the Dom
911 Feliciano/Kaoko Belt probably ended with an oblique collision and lateral escape or extrusion (Fernandes
912 et al., 1993; Tommasi et al., 1994; De Toni et al., 2021). The Kalahari Craton collision against the ‘Rio de
913 la Plata Craton-NPT’ assemblage (Philipp et al., 2016) was likely to occur during the last transpression
914 event (Goscombe et al., 2005; Oyhantçabal et al., 2011). This event produced tectonic constriction and
915 lateral extrusion of the NPT. Therefore, interspersed crustal slices coming from different origins are
916 expected (e.g., Burke and Şengör, 1986).

917 The structural evidence suggests that post-amalgamation tectonics produced subsequent brittle
918 reactivations, along with conjugate faults, like (1) Cuchilla del Rosario, sinistral, and (2) Cueva del Tigre,
919 dextral (Fig. 3).

920 The Neoproterozoic ductile deformation produced NE-SW foliations parallel to the Dom Feliciano Belt
921 (DFB) on Pavas Block’s eastern side. In contrast, it created the reactivation of older E-W structures in the
922 western region. Therefore, the Pavas and Cerro Chato Blocks seem to be allochthonous since the Santa
923 Lucia Granite (SL) has no equivalent in the Cerro Chato Block (Fig. 12). During the building of the DFB
924 (~600-550 Ma), there was an eastward-increasing deformation of the La China Complex and another
925 foreland basement. Strain-localisation through time gives rise to the Sierra Ballena Shear Zone in its
926 current form. The NPT separated into different lens-shaped blocks as soon as the reactivation of inherited
927 internal heterogeneities progressed. The Villa Serrana and Pavas blocks were the most involved in the
928 Neoproterozoic deformation. This region deformed at relatively low temperature during the
929 Neoproterozoic tectonic evolution. Therefore, high-grade metamorphic rocks are inherited from the pre-
930 orogenic foreland. Since then, the removal of large tectonic blocks adapted to accommodate the space

931 problem generated by the E-W shortening between the RPC and the Ralanian Craton during the Ediacaran.
932 This displacement caused rapid and drastic geometric changes in the Dom Feliciano Belt. An initial high
933 angle orientation probably parallel to the RPC's hypothetical northern edge. The Ediacaran orogenesis
934 deformed all the Mesoproterozoic and Neoproterozoic cover successions, except some detrital sequences
935 far away from the faults (e.g., Barriga Negra Formation). The displacement of crustal blocks during the
936 Neoproterozoic collision resulted in the Cerro Chato Block's insertion with an N-S shortening (Fig. 2).
937 However, this shortening could have been replaced by an N-S stretching through inversion tectonics
938 during the last Ediacaran transpressive event. In this new scheme, the Sarandí del Yí shear zone went from
939 dextral to sinistral movement. Meanwhile, its conjugate, the Maria Albina shear zone, went from sinistral
940 to dextral kinematics. The last transpressive event could produce the northwards lateral escape.

941 **5.3. Differences within the adjacent blocks and regional correlations**

942 *5.3.1. Geological differences between the NPT blocks*

943 A curved geological contact in the centre of the NPT is coincident with the Sierra de Sosa Shear Zone
944 (Fig. 3). The new map highlights a regional fold affecting the Pablo Paez sub-region (north of the Cerro
945 Chato Block) (Fig. 12). This fold would have developed during the Brasiliano orogenic event (Preciozzi et
946 al., 1979). The Neoproterozoic granites emplaced concordantly within the plastic reactivation of the gneiss
947 layering in the Cerro Chato Block. So far, only the Cerrezuelo granite has been dated at 619 Ma (Fort,
948 2020), but it emplaced within a hinge in the Cerro Chato Block. The Pablo Paez subregion may be the
949 continuation of the Pavas Block, as shown by the virgation of the Bouguer and magnetic anomalies (Fig.
950 4), despite the proposed disruption along the Tupambaé shear zone from different authors (Bates et al.,
951 2016; Oyhantcabal et al., 2018). The lithologies in the Pablo Paez subregion are orthogneisses and
952 intrusive granites (Preciozzi et al., 1979). Although retrogressed amphibolite facies rocks, there are traces
953 of iron formations, which resemble those of the Valentines Granulite Complex. Guillemin (1911) referred
954 to "walls of hematite-rich ferruginous rock" north of the Tupambaé railway station (Fig. 12). The geology
955 within the Valentines Granulite Complex has another equivalent in the Rivera block. Retrogressed
956 granulitic rocks, including para and orthogneisses, mafic rocks, and ca. 2.1 Ga blue quartz-bearing granites
957 are not present in the Pavas Block. Another difference between the blocks seems to be the lack of
958 Statherian (1.7-1.8 Ga) post-orogenic granitoids in Pavas. Although the Orosirian metamorphism (1.8-1.9
959 Ga) is common for the whole NPT, the Rhyacian granulite metamorphism and magmatism are lack in the
960 Pavas Block. Finally, there are similarities in the zircon detrital ages, as both carry on Rhyacian (2.1-2.2
961 Ga) and Archean (3.0 Ga) zircon ages to the Neoproterozoic deposits (Oyhantcabal et al., 2021). The
962 strips of shales, carbonate rocks and quartzites that survive erosion on the Cerro Chato block are absent
963 from the Pavas Block, except for some Ediacaran deposits with low strain. Finally, the Neo-
964 Archean/Siderian succession protoliths probably integrate the Valentines granulitic complex. The Villa
965 Serrana Block show traces of BIF and fuchsite-bearing quartzites in roof-pendants of Neoproterozoic
966 granites. The best-preserved Neo-Archean/Siderian succession is still the Las Tetas Complex and it is not
967 present in any other block.

969 The Pavas Block can be linked to the “Taquarembó Block” (Hartmann et al., 1999), the Luiz Alves
970 Terrane and the Santa Catarina Granulitic Complex in Southern Brazil (Hartmann et al., 1979; Basei et al.,
971 1992; Siga Jr., 1995). U-Pb zircon age (SHRIMP) at $2716 \pm 0,02$ Ga indicates Archean protoliths for the
972 Luiz Alves Terrane (Hartmann et al., 2000). The Luiz Alves Terrane has been subsequently deformed
973 during at least three different metamorphic events. A new investigation shows that U-Pb concordant zircon
974 ages range from 3.2 to 1.8 Ga, indicating a complex evolution (Heller et al., 2021). The titanite crystallised
975 at ca. 2.0 Ga, showing the retrograde path of the Orosirian metamorphism (Camboriú Orogeny). Reverse
976 discordant U-Pb zircon ages indicate that a hydrothermal alteration likely occurred during the
977 Neoproterozoic (Heller et al., 2021). Meanwhile, reverse discordant U-Pb zircon ages from the La China
978 Complex could be due to the same hydrothermalism. The Camboriú Orogeny (2.0-1.8 Ga) affected both
979 the Nico Pérez and Luiz Alves terranes. In Luiz Alves, the oldest inherited zircon age cluster is
980 Mesoarchean (ca. 3.2–3.1 Ga). Other populations yield Neoproterozoic magmatic ages (ca. 2.7-2.5 Ga). In the
981 Luiz Alves, many zircon grains crystallised during two high-grade metamorphic events at 2352 ± 23 Ma
982 and 2183 ± 17 Ma (Heller et al., 2021). However, the Rhyacian high-grade granulite event of the Rivera-
983 Valentines Complex (2.08 Ga) is younger. Conversely, the Pavas Block does not present any Rhyacian
984 granulitic metamorphism, and ca. 2.5-2.1 Ga old zircons are scarce (see Fig. 8). The Pavas Block shows
985 ~3.0 Ga magmatic crystallisation age from a minor granitoid group (Fig. 9e-f; Fig. 11), younger from the
986 basal La China Complex (≥ 3.1 Ga). The Pavas Block also includes Hbl-bearing granodiorite (sample
987 SY95; Annexe 1: Fig. 7a-f), which could be Neo-Archean (2.5-2.7 Ga) as well (not yet dated). Other U-Pb
988 zircon data confirmed Neo-Archean granitoids close to the Pavas Block’s eastern boundary. Gaucher et al.
989 (2014) found a magmatic age of ~2.7 Ga near the Sierra Ballena Shear Zone (sample FZ6; Table III,
990 Annexe 1). All these Neoproterozoic metagranitoids could be correlated to those of (i) the Atuba Complex
991 (Siga Jr. et al., 1995; Sato et al., 2003) and (ii) the Camboriú Complex (Basei et al., 2013) (Fig. 1). Most
992 magmatic protoliths in the Atuba Complex point to an age of ~3.0-2.9 Ga that was further affected by the
993 Camboriú orogenic event (~2.0 Ga) (Basei et al., 2013).

994 Concerning the Las Tetas Complex’s correlation, different cratonic successions could match with it in the
995 South American Platform. Lithological associations containing Cr-rich minerals (fuchsite, tourmaline),
996 like the Las Tetas Complex, were reported in the São Francisco Craton (e.g., Barbosa and Sabaté, 2002;
997 Milési et al., 2002; Albert et al., 2018). The Las Tetas Complex may resemble those of the Areião and
998 Contendas-Mirante on the Archean Gavião Block (Barbosa and Sabaté, 2002). The hydrothermal
999 alteration likely occurred in metasediments deposited during the Siderian/Rhyacian interval and succedent
1000 metamorphosed like metasedimentary rocks from the Caldeirão Belt (Oliveira et al., 2002). Meanwhile,
1001 the protolith succession of Las Tetas Complex has a maximum deposition age of 2764 ± 16 Ma (Hartmann
1002 et al., 2001), the detrital provenance of fuchsite quartzites and associated pelitic schists in the Caldeirão
1003 Belt is bracketed between 2076 and 2687 Ma by U-Pb SHRIMP in zircon (Oliveira et al., 2002).

1005 Geophysical data confirm the separation of the NPT into three blocks. Although brittle faults produced a
1006 late orogenic secondary reorganization, the consistency of the Pavas block depends on deeper ductile shear
1007 zones. The TCR map and the magnetic anomaly (dx1) confirm the dimensions and limits of the Pavas
1008 Block. The magnetic and gravimetric anomalies agree with its dimensions. The TCR map shows high
1009 radiometric contrast between the Pavas block and the others. It highlights the abundance of K-feldspar
1010 granites in the Cerro Chato Block, while in the Pavas block tonalitic gneisses predominate. Except for the
1011 Statherian Illescas granite, the other K-feldspar granites are Neoproterozoic and concordant with the
1012 regional gneissic layering. Some elements such as the Santa Lucía granite in the Pavas block are evidence
1013 of suspicious allochthony since there is no direct equivalent of this granite in the adjacent blocks. We
1014 found the suspicion on the different Paleoproterozoic history of the Pavas Block and the relative absence
1015 of Rhyacian and Statherian zircon ages. The southern edges of this block connect with transitional shear
1016 zones and the Mesoproterozoic schist belt named the Tapes Complex (Figs. 12, 13).

1017 The U-Pb zircon dating results indicate a predominance of Archean rocks (~2.7-3.4 Ga), followed by
1018 Orosirian magmatic and metamorphic age data (~1.8-2.0 Ga). The La China Complex shows three
1019 different zircon clusters: (i) Paleo-Archean (~3.3-3.1 Ga), (ii) Meso-Archean (~3.0-2.9 Ga) and (iii)
1020 Neoproterozoic (~2.7-2.8 Ga). Some zircon rim overgrowths display ~2.7 Ga ages. A reactivated flat-lying
1021 mylonite zone in the middle (CNP77) only provides Archean zircons. The thrusting probably occurred
1022 during a Paleoproterozoic tectonic event but was thermally reactivated likely during the Mesoproterozoic,
1023 which is blind for U-Pb in zircon methods. The southern part of the Pavas Block shows conspicuous
1024 Orosirian metamorphism near the contact with the Villa Serrana Block. Zircons yield concordant ~1.8-1.9
1025 Ga U-Pb ages in the overgrowth, interpreted as the partial melt crystallisation, but the magmatic protolith
1026 is Archean. A crustal melting S-type granitoid (e.g., Arroyo Perdido Granite) yields an Orosirian age but
1027 extremely negative ϵ_{Hf} and Archean TDM model age, confirming the presence of Archean protoliths near
1028 the southern end (i.e., Minas town). Archean rocks affected by hydrothermalism are widespread, probably
1029 related to the Orosirian metamorphic event. Some gneisses show zircon annealing which can be
1030 interpreted as produced by radioactive-damaged recovering assisted by fluids. This process must occur
1031 during the retrogressive path and does not involve Pb-loss. An Orosirian K-feldspar granite (~2.0 Ga)
1032 without any Archean heritage underwent Neoproterozoic deformation along the flat-lying, strike-slip
1033 Espuelitas lateral ramp (Fig. 12). This granite likely set the southern end of the block in a transitional
1034 crust. The discovery of a foliated granodiorite crosscutting the La China Complex suggested that later
1035 Neoproterozoic granitoids can be separated from the basal complex. Neoproterozoic/Siderian metasediments are
1036 thrust on the La China Complex, producing strong N-S stretching lineations parallel to the Dom
1037 Feliciano Belt. This succession appears as far as the southern end of the Pavas Block, mostly represented
1038 by fuchsite-bearing quartzites / metaconglomerates, carbonates, BIF and amphibolites.

1039 **Acknowledgements**

1040 We thank Bruna Sanches, Nairé Gabriel, and the rest of the team at the Centro de Pesquisas
 1041 Geocronológicas of the University of São Paulo. We thank Dr Elena Peel for the help regarding the use of
 1042 standard deviation in the Concordia diagram. We are also indebted to the Director Lic. Nestor Campal,
 1043 who authorized the use of the airborne geophysical data of DINAMIGE for academic purposes. The
 1044 authors are grateful to CSIC (UdelaR) for the funding granted (project CSIC-2015 C-604) and to the
 1045 Faculty of Sciences of the Universidad de la República (Uruguay) for the Logistics. They also
 1046 acknowledge PEDECIBA - Geosciences who provided grants. To Ecos-sud Conicyt program n°U17U01
 1047 for funding the travels and per diem to Tahar Aïfa and Henri Masquelin through a cooperation exchange
 1048 program between the Rennes 1 and UdelaR universities since 2018. This work is also a contribution to the
 1049 Unesco-igcp638 program.

1050 **REFERENCES**

- 1051 Albert, C., Lana, C., Gerdes, A., Schannor, M., Narduzzi, F., Queiroga, G. (2018). Archean magmatic-
 1052 hydrothermal fluid evolution in the Quadrilátero Ferrífero (SE Brazil) documented by B isotopes (LA
 1053 MC-ICPMS) in tourmaline. *Chemical Geology*, 481, 95-109.
- 1054 Almeida, F.F.M. de, Amaral, G., Cordani, U., Kawashita, K. (1973). The Precambrian evolution of the
 1055 South American cratonic margin south of the Amazon River. *In: The South Atlantic* (pp. 411-446).
 1056 Springer, Boston, MA.
- 1057 Ávila, C.A., Teixeira, W., Cordani, U.G., Moura, C.A.V., Pereira, R.M. (2010). Rhyacian (2.23–2.20 Ga)
 1058 juvenile accretion in the southern São Francisco craton, Brazil: Geochemical and isotopic evidence
 1059 from the Serrinha magmatic suite, Mineiro belt. *Journal of South American Earth Sciences*, 29(2),
 1060 464-482.
- 1061 Babinski, M., Chemale Jr, F., Van Schmus, W. R., Hartmann, L. A., Da Silva, L.C. (1997). U-Pb and Sm-
 1062 Nd geochronology of the Neoproterozoic granitic-gneissic Dom Feliciano Belt, southern Brazil.
 1063 *Journal of South American Earth Sciences*, 10(3-4), 263-274.
- 1064 Barbosa, J.S., Sabaté, P. (2002). Geological features and the Paleoproterozoic collision of four Archean
 1065 crustal segments of the São Francisco Craton, Bahia, Brazil: a synthesis. *Anais da Academia
 1066 Brasileira de Ciências*, 74(2), 343-359.
- 1067 Basei, M.A.S., Siga Jr., O., Machiavelli, A., Mancini, F., (1992). Evolução Tectônica dos Terrenos entre os
 1068 Cinturões Ribeira e Dom Feliciano (PR-SC). *Revista Brasileira de Geociências*, 22(2), 216-221.
- 1069 Basei, M.A.S., Siga Jr, O., Masquelin, H., Harara, O.M., Reis Neto, J.M., Preciozzi, F. (2000). *The Dom
 1070 Feliciano Belt (Brazil – Uruguay) and its foreland (Rio de la Plata Craton): Framework, Tectonic
 1071 Evolution and Correlations with similar terranes of Southwestern Africa*. *In: Cordani, Thomaz Fº
 1072 Milani (eds.), Precambrian Evolution of South America*. 31st Int. Geol. Congr., IUGS, Rio de Janeiro,
 1073 Brazil, 2000, 311-334.
- 1074 Basei, M.A.S., Frimmel, H.E., Nutman, A.P., Preciozzi, F., Jacob, J. (2005). The connection between the
 1075 Neoproterozoic Dom Feliciano (Brazil/Uruguay) and Gariep (Namibia/South Africa) orogenic belts.
 1076 *Precambrian Research*, 139, 139-221.
- 1077 Basei, M.A.S., Frimmel, H.E., Nutman, A.P., Preciozzi, F. (2008). West Gondwana amalgamation based
 1078 on detrital zircon ages from Neoproterozoic Ribeira and Dom Feliciano belts of South America and
 1079 comparison with coeval sequences from SW Africa. *Geological Society, London, Special
 1080 Publications*, 294(1), 239-256.
- 1081 Basei, M.A.S., Campos Neto, M.D.C., Lopes, A.P., Nutman, A.P., Liu, D., Sato, K. (2013). Polycyclic
 1082 evolution of Camboriú Complex migmatites, Santa Catarina, Southern Brazil: integrated Hf isotopic

- 1083 and U-Pb age zircon evidence of episodic reworking of a Mesozoic juvenile crust. *Brazilian*
1084 *Journal of Geology*, 43(3), 427-443.
- 1085 Bates, M., McLeish, M., Mushayandebvu, M. (2016). *Interpretation report: Partial airborne geophysical*
1086 *survey of the national territory and the procedure and interpretation of existing geophysical data.*
1087 Sander Geophysics Ltd., Contract No. 01/2013, Report for DINAMIGE, 1-654, Ottawa, Canada.
- 1088 Bekker, A., Holland, H. D., Wang, P. L., Rumble, D.I.I., Stein, H.J., Hannah, J.L., ... Beukes, N.J. (2004).
1089 Dating the rise of atmospheric oxygen. *Nature*, 427(6970), 117-120.
- 1090 Blanco, G., Rajesh, H. M., Gaucher, C., Germs, G. J., Chemale Jr, F. (2009). Provenance of the Arroyo
1091 del Soldado Group (Ediacaran to Cambrian, Uruguay): implications for the paleogeographic evolution
1092 of southwestern Gondwana. *Precambrian Research*, 171(1-4), 57-73.
- 1093 Bologna, M.S., Dragone, G.N., Muzio, R., Peel, E., Nuñez-Demarco, P., Ussami, N. (2019). Electrical
1094 structure of the lithosphere from Rio de la Plata craton to Paraná basin: Amalgamation of cratonic and
1095 refertilized lithospheres in SW Gondwanaland. *Tectonics*, 38(1), 77-94.
- 1096 Bossi, J., Campal, N., 1991. *Granitos negros filonianos del Uruguay: Resultados de las investigaciones.*
1097 *In: Proyecto "Granito Negro".* Convenio CIID - UdelaR, IDRC - Archivo 90650, 72p.
- 1098 Bossi, J., Campal, N. (1992). *Magmatismo y tectónica transcurrente durante el Paleozoico inferior en*
1099 *Uruguay.* In: Gutiérrez Marco, J.C., Saavedra, J., Rábano, I. (Eds.), *Paleozoico inferior de*
1100 *Iberoamérica.* Universidad de Extremadura, España, 343-356.
- 1101 Bossi, J., Ferrando, L., Montaña, J., Campal, N., Morales, H., Gancio, F., Schipilov, A., Piñeyro, D.,
1102 Sprechmann, P. (2001). *Memoria explicativa de la Carta Geológica del Uruguay a escala 1:500.000.*
1103 Fac. Agronomía - UdelaR, 1-122.
- 1104 Bossi, J., Gaucher, C. (2004). The Cuchilla Dionisio Terrane, Uruguay: An Allochthonous Block Accreted
1105 in the Cambrian to SW-Gondwana. *Gondwana Research*, 7(3), 661-674. [doi: 10.1016 / S1342 - 937X
1106 (05)71054-6].
- 1107 Brito Neves, B.B. de, Cordani, U.G. (1991). Tectonic evolution of South-America during the late
1108 Proterozoic. *Precambrian Research*, 53(1-2), 23-40.
- 1109 Brito Neves, B.B. de, Campos Neto, M.D.C., Fuck, R.A. (1999). From Rodinia to Western Gondwana: an
1110 approach to the Brasiliano-Pan African Cycle and orogenic collage. *Episodes*, IUGS, 22(3), 155-166.
- 1111 Brito Neves, B.B. de (2011). The Paleoproterozoic in the South American continent: diversity in the
1112 geologic time. *Journal of South American Earth Sciences*, 32(4), 270-286.
- 1113 Brito Neves, B.B. de, Fuck, R.A., Pimentel, M.M. (2014). The Brasiliano collage in South America: a
1114 review. *Brazilian Journal of Geology*, 44(3), 493-518.
- 1115 Bruno, H., Heilbron, M., de Morisson Valeriano, C., Strachan, R., Fowler, M., Bersan, S., ... Storey, C.
1116 (2021). Evidence for a complex accretionary history preceding the amalgamation of Columbia: The
1117 Rhyacian Minas-Bahia Orogen, southern São Francisco Paleocontinent, Brazil. *Gondwana Research*,
1118 92, 149-171.
- 1119 Burke, K., Şengör, C. (1986). Tectonic escape in the evolution of the continental crust. *In: Reflection*
1120 *seismology: the continental crust*, AGU Geodynamics Series, Vol. 14, 41-53.
- 1121 Campal, N., Schipilov, A. (1995). The Illescas bluish-quartz rapakivi granite (Uruguay-South America):
1122 some geological features. *In: Symposium of rapakivi granites and related rocks:* Belém, Brasil.
1123 *Abstracts*, p. 18.
- 1124 Campal, N., Schipilov, A. (1999). The eastern edge of the Rio de la Plata Craton: a history of tangential
1125 collisions. *In: Basement Tectonics*, 13 (pp. 33-48). Springer, Dordrecht.
- 1126 Campos Neto, M.C. (2000). Orogenic systems from southwestern Gondwana. An approach to Brasiliano-
1127 Pan African cycle and orogenic collage in south-eastern Brazil. *In: Cordani, U., Milani, E., Thomaz*
1128 *Filho, A., and Campos, D. (Eds.), Tectonic evolution of South America.* Rio Janeiro, pp. 335-365.
- 1129 Cawood, P.A., Buchan, C. (2007). Linking accretionary orogenesis with supercontinent assembly. *Earth-*
1130 *Science Reviews*, 82(3-4), 217-256.
- 1131 Clark, C., Hand, M., Kelsey, D.E., Goscombe, B. (2007). Linking crustal reworking to terrane accretion.
1132 *Journal of the Geological Society*, 164(5), 937-940.

- 1133 Condie, R.C., Aster, R.C. (2010). Episodic zircon age spectra of Proterozoic granitoids: the supercontinent
1134 connection and continental growth. *Precambrian Research*, 180(3-4), 227-236.
- 1135 Cordani, U.G., Brito-Neves, B.B., D'Agrella-Filho, M.S. (2003). From Rodinia to Gondwana: a review of
1136 the available evidence from South America. *Gondwana Research*, 6(2), 275-283.
- 1137 Corfu, F., Hanchar, J.M., Hoskin, P.W., Kinny, P. (2003). Atlas of zircon textures. *Reviews in mineralogy
1138 and geochemistry*, 53(1), 469-500.
- 1139 Crowley, J.L., Myers, J.S., Dunning, G.R. (2002). Timing and nature of multiple 3700–3600 Ma tectonic
1140 events in intrusive rocks north of the Isua greenstone belt, southern West Greenland. *Geological
1141 Society of America Bulletin*, 114(10), 1311-1325.
- 1142 Da Silva, L.C., McNaughton, N.J., Fletcher, I.R. (2005). SHRIMP U–Pb zircon geochronology of
1143 Neoproterozoic crustal granitoids (Southern Brazil): a case for discrimination of emplacement and
1144 inherited ages. *Lithos*, 82(3-4), 503-525.
- 1145 DeCelles, P.G., Ducea, M.N., Kapp, P., Zandt, G. (2009) Cyclicity in Cordilleran orogenic systems.
1146 *Nature Geoscience*, 2: 251-257.
- 1147 De Silva, S.L., Riggs, N.R., Barth, A.P. (2015). Quickening the pulse: fractal tempos in continental arc
1148 magmatism. *Elements*, 11(2), 113-118.
- 1149 De Toni, G.B., Bitencourt, M.F., Konopásek, J., Battisti, M.A., da Costa, E.O., Savian, J.F. (2021).
1150 Autochthonous origin of the Encruzilhada Block, Dom Feliciano Belt, southern Brazil, based on aero-
1151 geophysics, image analysis and PT-paths. *Journal of Geodynamics*, 101825.
- 1152 Ducea, M.N., Paterson, S. R., DeCelles, P. G. (2015). High-volume magmatic events in subduction
1153 systems. *Elements*, 11(2), 99-104.
- 1154 Fambrini, G.L., Fragoso-Cesar, A.R.S., de Almeida, R.P., Riccomini, C. (2005). A Formação Barriga
1155 Negra (Ediacarano do Uruguai): caracterização estratigráfica e correlação com unidades do estado do
1156 Rio Grande do Sul, Brasil. *Revista Brasileira de Geociências*, 35(4), 515-524.
- 1157 Fernandes, L.A.D., Tommasi, A., Porcher, C. (1992). Deformation patterns in the Southern Brazilian
1158 Branch of the Dom Feliciano Belt: A reappraisal. *Journal of South American Earth Sciences*, 5(1), 77-
1159 96.
- 1160 Fernandes, L.A.D., Tommasi, A., Vauchez, A., Porcher, C. C., Menegat, R., Koester, E. (1993). Zona de
1161 Cisalhamento Transcorrente Dorsal de Canguçu: caracterização e importância na compartimentação
1162 tectônica do Cinturão Dom Feliciano. *Revista Brasileira de Geociências*, 23(3), 224-233.
- 1163 Fernandes, L.A.D., Menegat, R., Costa, A.F.U., Koester, E., Porcher, C.C., Tommasi, A., Kramer, G.,
1164 Ramgrab, G., Camozzato, E. (1995). Evolução Tectônica do Cinturão Dom Feliciano no Escudo Sul-
1165 Rio-Grandense: Parte I - Uma Contribuição a partir do registro Geológico. *Revista Brasileira de
1166 Geociências*, 25(4), 351-374.
- 1167 Fort, S. (2020). *Petrografía, geoquímica e isotopía del magmatismo granítico neoproterozoico del Centro-
1168 Noreste de Uruguay*. PEDECIBA-Geociencias, UdelaR. MSc Thesis, pp. 1-145.
- 1169 Fragoso Cesar, A.R.S. 1980. O Cráton do Rio de La Plata e o Cinturão Dom Feliciano no Escudo
1170 Uruguaio-Sul-Riograndense. In: *Congresso Brasileiro de Geologia*, 31, Camboriú, 1980. Anais,
1171 SBG,5:2879-2892.
- 1172 Frei, R., Rosing, M.T., Waight, T.E., Ulfbeck, D.G. (2002). Hydrothermal-metasomatic and tectono-
1173 metamorphic processes in the Isua supracrustal belt (West Greenland): A multi-isotopic investigation
1174 of their effects on the Earth's oldest oceanic crustal sequence. *Geochimica et Cosmochimica Acta*,
1175 66(3), 467-486.
- 1176 Frimmel, H.E., Basei, M.S., Gaucher, C. (2011). Neoproterozoic geodynamic evolution of SW-
1177 Gondwana: a southern African perspective. *International Journal of Earth Sciences*, 100(2), 323-354.
- 1178 Gaucher, C., Finney, S.C., Poiré, D.G., Valencia, V.A., Grove, M., Blanco, G., ... Peral, LG (2008).
1179 Detrital zircon ages of Neoproterozoic sedimentary successions in Uruguay and Argentina: insights
1180 into the geological evolution of the Río de la Plata Craton. *Precambrian Research*, 167(1-2), 150-170.
- 1181 Gaucher, C., Frei, R., Chemale, F., Frei, D., Bossi, J., Martínez, G., Chigolino, L., Cernuschi, F. (2011).
1182 Mesoproterozoic evolution of the Río de la Plata Craton in Uruguay: at the heart of Rodinia?
1183 *International Journal of Earth Sciences*, 100(2-3), 273-288.

- 1184 Gaucher, C., Bossi, J., Chemale Jr, F., García, G., Frei, R., Frei, D. (2014a). Complejo La Chimia, las locas
1185 más antiguas de Uruguay. In: Bossi, J. & Gaucher, C. (eds.), *Geología del Uruguay*, v. 1: chp. 5, 141-
1186 154.
- 1187 Gaucher, C., Frei, R., Sial, A.N., Castiglioni, E., Ferreira, V.P. (2014b). Grupo Cebollatí. In: Bossi, J. &
1188 Gaucher, C. (eds.), *Geología del Uruguay*, v. 1: chp. 6, 155-169.
- 1189 Gaucher, C., Frei, R., Will, T., Samaniego, L., Ling, X.X., Li, X.H., Li, Q.-L. (2019). Complejo Tapes
1190 (Terreno Nico Pérez): Edad y relación con otras unidades del Mesoproterozoico de Uruguay. In: 9°
1191 Congreso Uruguayo de Geología. Trinidad (4 al 8 Nov): Soc. Urug. Geol., Resúmenes, p. 57.
- 1192 Geisler, T., Pidgeon, R.T., Van Bronswijk, W., Kurtz, R. (2002). Transport of uranium, thorium, and lead
1193 in metamict zircon under low-temperature hydrothermal conditions. *Chemical Geology*, 191(1-3),
1194 141-154.
- 1195 Geisler, T., Pidgeon, R.T., Kurtz, R., Van Bronswijk, W., Schleicher, H. (2003). Experimental
1196 hydrothermal alteration of partially metamict zircon. *American Mineralogist*, 88(10), 1496-1513.
- 1197 Geisler, T., Schaltegger, U., Tomaschek, F. (2007). Re-equilibration of zircon in aqueous fluids and melts.
1198 *Elements*, 3(1), 43-50.
- 1199 Ginster, U., Reiners, P. W., Nasdala, L., Chanmuang, C. (2019). Annealing kinetics of radiation damage in
1200 zircon. *Geochimica et Cosmochimica Acta*, 249, 225-246.
- 1201 Girelli, T.J., Chemale Jr, F., Lavina, E.L.C., Laux, J.H., Bongiolo, E.M., Lana, C. (2018). Granulite
1202 accretion to Rio de la Plata Craton, based on zircon U-Pb-Hf isotopes: Tectonic implications for
1203 Columbia Supercontinent reconstruction. *Gondwana Research*, 56, 105-118.
- 1204 Goscombe, B., Gray, D., Hand, M. (2005). Extrusion tectonics in the core of a transpressional orogen; the
1205 Kaoko Belt, Namibia. *Journal of Petrology*, 46(6), 1203-1241.
- 1206 Goscombe, B., Gray, D.R. (2007). The Coastal Terrane of the Kaoko Belt, Namibia: outboard arc-terrane
1207 and tectonic significance. *Precambrian Research*, 155(1-2), 139-158.
- 1208 Grimes, C.B., Wooden, J.L., Cheadle, M.J., John, B.E. (2015). “Fingerprinting” tectono-magmatic
1209 provenance using trace elements in igneous zircon. *Contributions to Mineralogy and Petrology*,
1210 170(5), 1-26.
- 1211 Guerrero, S. (2016). *Geología, petrografía y aspectos macro-, meso-, y microestructurales del área del*
1212 *Salto del Penitente*. Trabajo final de Licenciatura en Geología, UdelaR, 94 p.
- 1213 Guillemain, C. (1911). Zur Geologie Uruguays. *Zeitschr. Deutsch Geol. Ges.*, Berlin, Bd. 63(4), 203-220.
- 1214 Harley, S.L., Kelly, N.M., Möller, A. (2007). Zircon behaviour and the thermal histories of mountain
1215 chains. *Elements*, 3(1), 25-30.
- 1216 Hartmann, L.A., Silva, L.C., Orlandi Filho, V. (1979). O Complexo Granulítico de Santa Catarina.
1217 Descrição e implicações genéticas. *Acta Geologica Leopoldensia*, 3(6), 93-112.
- 1218 Hartmann, L.A., Leite, J.A.D., McNaughton, N.J., Santos, J.O.S. (1999). Deepest exposed crust of Brazil
1219 – SHRIMP establishes three events. *Geology*, 27(10), 947–950.
- 1220 Hartmann, L.A., Santos, J.O.S., McNaughton, N.J., Vasconcellos, M.A.Z., Da Silva, L.C. (2000). Ion
1221 microprobe (SHRIMP) dates complex granulite from Santa Catarina, Southern Brazil. *Anais da*
1222 *Academia Brasileira de Ciências*. 72, 559-572.
- 1223 Hartmann, L.A., Campal, N., Santos, J.O.S., McNaughton, N.J., Schipilov, A. (2001). Archaean crust in
1224 the Río de la Plata Craton, Uruguay: SHRIMP U–Pb reconnaissance geochronology. *Journal of South*
1225 *American Earth Sciences*, 14, 557–570.
- 1226 Hasui, Y. (1982). The Mantiqueira province: Archean structure and Proterozoic evolution. *Revista*
1227 *Brasileira de Geociências*, 12(1-3), 167-171.
- 1228 Heller, B.M., Hueck, M., Passarelli, C.R., Basei, M.A.S. (2021). Zircon U-Pb geochronology and Hf
1229 isotopes of the Luís Alves Terrane: Archean to Paleoproterozoic evolution and Neoproterozoic
1230 overprint. *Journal of South American Earth Sciences*, 106, DOI: 10.1016/j.jsames.2020.103008.
- 1231 Hoskin, P.W.O., Black, L.P. (2000). Metamorphic zircon formation by solid-state recrystallization of
1232 protolith igneous zircon. *Journal of Metamorphic Geology*, 18(4), 423-439.

- 1233 Hoskin, P.W.O., Schaltegger, G. (2005). The composition of zircon and igneous and metamorphic
1234 petrogenesis. *Reviews in mineralogy and geochemistry*, 53(1), 27-62.
- 1235 Hueck, M., Oyhantçabal, P., Philipp, R.P., Basei, M.A.S., Siegesmund, S. (2018). The Dom Feliciano Belt
1236 in southern Brazil and Uruguay. *In: Geology of Southwest Gondwana* (pp. 267-302). Springer, Cham.
- 1237 Jost, H., Hartmann, L. A. (1984). *Província Mantiqueira-Setor Meridional*. *In: F.F.M. de Almeida (Ed.),*
1238 *O Pré-Cambriano do Brasil*, 345-68. Edgard Blücher Ltd., São Paulo.
- 1239 Kielman, R.B., Nemchin, A.A., Whitehouse, M.J., Pidgeon, R.T., Bellucci, J.J. (2018). U-Pb age
1240 distribution recorded in zircons from Archean quartzites in the Mt. Alfred area, Yilgarn Craton,
1241 Western Australia. *Precambrian Research*, 310, 278-290.
- 1242 Kohn, M.J., Kelly, N.M. (2018). Petrology and geochronology of metamorphic zircon, chapter 2. *In:*
1243 *Microstructural geochronology: Planetary records down to atom scale* (Moser et al., eds.),
1244 Geophysical Monograph Series, AGU, 35-61.
- 1245 Konhauser, K.O., Lalonde, S.V., Planavsky, N.J., Pecoits, E., Lyons, T.W., Mojzsis, S.J., ... Bekker, A.
1246 (2011). Aerobic bacterial pyrite oxidation and acid rock drainage during the Great Oxidation Event.
1247 *Nature*, 478(7369), 369-373.
- 1248 Lara, P., Oyhantçabal, P., Belousova, E. (2020). Two distinct crustal sources for Late Neoproterozoic
1249 granitic magmatism across the Sierra Ballena Shear Zone, Dom Feliciano Belt, Uruguay: Whole-rock
1250 geochemistry, zircon geochronology and Sr-Nd-Hf isotope evidence. *Precambrian Research*, 341,
1251 105625.
- 1252 Lee, D.E., Bastron, H. (1967). Fractionation of rare-earth elements in allanite and monazite as related to
1253 the geology of the Mt. Wheeler mine area, Nevada. *Geochimica et Cosmochimica Acta*, 31(3), 339-
1254 356.
- 1255 Lee, J.K., Tromp, J. (1995). Self-induced fracture generation in zircon. *Journal of Geophysical Research:*
1256 *Solid Earth*, 100(B9), 17753-17770.
- 1257 Loureiro J., Silva, H., Sánchez Bettucci, L. (2019). Mapa Geológico: El Arqueano en el Uruguay, *Revista*
1258 *Investigaciones*, Montevideo, 2(1), 28-3.
- 1259 Mallmann, G., Chemale Jr, F., Ávila, J.N., Kawashita, K., Armstrong, R.A. (2007). Isotope geochemistry
1260 and geochronology of the Nico Perez terrane, Rio de la Plata craton, Uruguay. *Gondwana Research*,
1261 12(4), 489-508.
- 1262 Martins-Ferreira, M.A.C., Dias, A.N.C., Chemale Jr, F., Campos, J.E.G., Seraine, M., Novais-Rodrigues,
1263 E. (2020). Multi-stage crustal accretion by magmatic flare-up and quiescence intervals in the western
1264 margin of the São Francisco Craton: U-Pb-Hf and geochemical constraints from the Almas Terrane.
1265 *Gondwana Research*, 85, 32-54.
- 1266 Masquelin, H. (2006). El Escudo Uruguayo. *In: Cuencas Sedimentarias del Uruguay: Paleozoico*
1267 *(Veroslavsky et al., eds.)*, 3, 37-106. DIRAC, UdelaR.
- 1268 Masquelin H., Silva Lara, H., Sánchez Bettucci, L., Núñez Demarco, P., Pascual, S., Muzio, R., Peel, E.,
1269 Scaglia, F. (2017). Lithologies, structure and basement-cover relationships in the schist belt of the Dom
1270 Feliciano Belt in Uruguay. *Brazilian Journal of Geology*, 47(1), 21-42.
- 1271 Mezger, K., Krogstad, E. J. (1997). Interpretation of discordant U-Pb zircon ages: An evaluation. *Journal*
1272 *of Metamorphic Geology*, 15(1), 127-140.
- 1273 Midot, D. (1984): *Étude géologique et diagnostique métallogénique pour l'exploration du secteur de*
1274 *Minas, Uruguay*. Thèse Doctorat 3ème Cycle, Univ. Paris VI, 1 vol.: 84/24, pp. 1-175.
- 1275 Montaña, J., Sprechmann, P. (1993). Calizas estromatolíticas y oolíticas y definición de la Formación
1276 Arroyo de la Pedrera (Vendiano, Uruguay). *Revista Brasileira de Geociências*, 23(3), 306-312.
- 1277 Montel, J.M. (1993). A model for monazite/melt equilibrium and application to the generation of granitic
1278 magmas. *Chemical Geology*, 110(1-3), 127-146.
- 1279 Milési, J.P., Ledru, P., Marcoux, E., Mougeot, R., Johan, V., Lerouge, C., ... Skipwith, P. (2002). The
1280 Jacobina Paleoproterozoic gold-bearing conglomerates, Bahia, Brazil: a "hydrothermal shear-
1281 reservoir" model. *Ore Geology Reviews*, 19(1-2), 95-136.
- 1282 Murphy, J.B., Nance, R.D. (1991). Supercontinent model for the contrasting character of Late Proterozoic
1283 orogenic belts. *Geology*, 19(5), 469-472.

- 1284 Nasuara, E., Wenzel, M., Vavra, G., Hübner, G., Wenzel, T., Kober, B. (2001). Metamictization of natural
 1285 zircon: accumulation versus thermal annealing of radioactivity-induced damage. *Contributions to*
 1286 *Mineralogy and Petrology*, 141(2), 125-144.
- 1287 Núñez Demarco, P. (2019). Litodema Tarumán Una secuencia metasedimentaria arqueana del Uruguay.
 1288 *Revista Investigaciones*, Montevideo, 2(2), 41-53.
- 1289 Nutman, A.P., Maciejowski, R., Wan, Y. (2014). Protoliths of enigmatic Archaean gneisses established
 1290 from zircon inclusion studies: A case study of the Caozhuang quartzite, E. Hebei, China. *Geoscience*
 1291 *Frontiers*, 5(4), 445-455.
- 1292 Oliveira, E.P., Mello, E.F., McNaughton, N. (2002). Reconnaissance U-Pb geochronology of Precambrian
 1293 quartzites from the Caldeirão belt and their basement, NE São Francisco Craton, Bahia, Brazil:
 1294 implications for the early evolution of the Paleoproterozoic Itabuna-Salvador-Curaçá orogen. *Journal*
 1295 *of South American Earth Sciences*, 15(3), 349-362.
- 1296 Oriolo, S., Oyhantçabal, P., Wemmer, K., Heidelbach, F., Pfänder, J., Basei, M. A., ... Siegesmund, S.
 1297 (2015). Shear zone evolution and timing of deformation in the Neoproterozoic transpressional Dom
 1298 Feliciano Belt, Uruguay. *Journal of Structural Geology*, 92, 59-78.
- 1299 Oriolo, S., Oyhantçabal, P., Basei, M. A., Wemmer, K., Siegesmund, S. (2016a). The Nico Pérez Terrane
 1300 (Uruguay): from Archean crustal growth and connections with the Congo Craton to late
 1301 Neoproterozoic accretion to the Río de Rio de la Plata Craton. *Precambrian Research*, 280, 147-160.
- 1302 Oriolo, S., Oyhantçabal, P., Wemmer, K., Basei, M. A., Benowitz, J., Pfänder, J., ... Siegesmund, S.
 1303 (2016b). Timing of deformation in the Sarandí del Yí Shear Zone, Uruguay: Implications for the
 1304 amalgamation of western Gondwana during the Neoproterozoic Brasiliano □ Pan □ African Orogeny.
 1305 *Tectonics*, AGU, 35(3), 754-771.
- 1306 Oriolo, S., Oyhantçabal, P., Konopásek, J., Basei, M. A., Frei, R., Sláma, J., Wemmer, K., Siegesmund, S.
 1307 (2019). Late Paleoproterozoic and Mesoproterozoic magmatism of the Nico Pérez Terrane (Uruguay):
 1308 Tightening up correlations in southwestern Gondwana. *Precambrian Research*, 327, 296-313.
 1309 [doi.org/10.1016/j.precamres.2019.04.012].
- 1310 Oyhantçabal, P., Vaz Chaves, N. (1990). Una asociación de cuarcitas y rocas máficas y ultramáficas en los
 1311 alrededores de Isla Patrulla (Departamento de Treinta y Tres). Resúmenes ampliados del Primer
 1312 Congreso Uruguayo de Geología. In: *Congreso Uruguayo de Geología*, I. Montevideo, 25-27 abr.
 1313 1990, Actas.
- 1314 Oyhantçabal, P., Muzio, R., De Souza, S. (1993). Geología y aspectos estructurales del borde orogénico en
 1315 el extremo sur del cinturón Dom Feliciano. *Revista Brasileira de Geociências*, 23(3), 296-300.
- 1316 Oyhantçabal, P., Siegesmund, S., Wemmer, K., Frei, R., Layer, P. (2007). Post-collisional transition from
 1317 calc-alkaline to alkaline magmatism during transcurrent deformation in the southernmost Dom
 1318 Feliciano Belt (Brasiliano - Pan-African, Uruguay). *Lithos*, 98(1-4), 141-159.
- 1319 Oyhantçabal, P., Siegesmund, S., Wemmer, K., Presnyakov, S., Layer, P. (2009). Geochronological
 1320 constraints on the evolution of the southern Dom Feliciano Belt (Uruguay). *Journal of the Geological*
 1321 *Society*, 166(6), 1075-1084.
- 1322 Oyhantçabal P., Siegesmund, S., Wemmer, K., Passchier, C.W. (2011). The transpressional connection
 1323 between Dom Feliciano and Kaoko Belts at 580-550 Ma. *International Journal of Earth Sciences*
 1324 (*Geol. Rundsch.*), 100(2-3): 379-390.
- 1325 Oyhantçabal, P., Wagner-Eimer, M., Wemmer, K., Schulz, B., Frei, R., Siegesmund, S. (2012). Paleo- and
 1326 Neoproterozoic magmatic and tectonometamorphic evolution of the Isla Cristalina de Rivera (Nico
 1327 Pérez Terrane, Uruguay). *International Journal of Earth Sciences (Geol. Rundsch.)*, 101(7), 1745-
 1328 1762.
- 1329 Oyhantçabal, P., Oriolo, S., Philipp, R. P., Wemmer, K., Siegesmund, S. (2018). The Nico Pérez Terrane
 1330 of Uruguay and South-Eastern Brazil. In: *Geology of Southwest Gondwana* (pp. 161-188). Springer,
 1331 Cham.
- 1332 Oyhantçabal, P., Oriolo, S., Wemmer, K., Basei, M.A.S., Frei, D., Siegesmund, S. (2021). Provenance of
 1333 metasedimentary rocks of the western Dom Feliciano Belt in Uruguay: Insights from U–Pb detrital
 1334 zircon geochronology, Hf and Nd model ages, and geochemical data. *Journal of South American*
 1335 *Earth Sciences*, 108, 103139.

- 1336 Pecois, E., Abuel, N. R., Heaman, L. M., Philippot, F., Rosiè, C. A., Veroslavsky, G., Kommauer, R.O.
 1337 (2016). U-Pb detrital zircon ages from some Neoproterozoic successions of Uruguay: Provenance,
 1338 stratigraphy, and tectonic evolution. *Journal of South American Earth Sciences*, 71, 108-130.
- 1339 Peel, E., Bettucci, L.S., Basei, M.A.S. (2018). Geology and geochronology of Paso del Dragón Complex
 1340 (north-eastern Uruguay): implications on the evolution of the Dom Feliciano Belt (Western
 1341 Gondwana). *Journal of South American Earth Sciences*, 85, 250-262.
- 1342 Philipp, R.P., Pimentel, M.M., Chemale Jr, F. (2016). Tectonic evolution of the Dom Feliciano Belt in
 1343 southern Brazil: Geological relationships and U-Pb geochronology. *Brazilian Journal of Geology*, 46,
 1344 83-104.
- 1345 Pidgeon, R.T. (1992). Recrystallization of oscillatory zoned zircon: some geochronological and
 1346 petrological implications. *Contributions to Mineralogy and Petrology*, 110(4), 463-472.
- 1347 Pidgeon, R.T., Nemchin, A.A., Hitchen, G.J. (1998). Internal structures of zircons from Archaean granites
 1348 from the Darling Range batholith: implications for zircon stability and the interpretation of zircon U-
 1349 Pb ages. *Contributions to Mineralogy and Petrology*, 132(3), 288-299.
- 1350 Pidgeon, R.T., Nemchin, A.A., Kinny, P.D. (2000). Fir-tree and nebulously zoned zircons from granulite-
 1351 facies rocks: Evidence for zircon growth and interaction with metamorphic fluids. *Goldschmidt 2000*.
 1352 Int. J. Conf. Abstr. (Vol. 5, p. 798).
- 1353 Pearce, J.A. (2014). Geochemical fingerprinting of the Earth's oldest rocks. *Geology*, 42(2), 175-176.
- 1354 Preciozzi, F., Spoturno, J., Heinzen, W. (1979). *Carta geo-estructural del Uruguay, escala 1:2.000.000*.
 1355 Instituto Geológico Ing. Terra Arocena, Montevideo, 76 p.
- 1356 Preciozzi, F., Spoturno, J., Heinzen, W., Rossi, P. (1985). *Memoria Explicativa de la Carta Geológica del*
 1357 *Uruguay a la escala 1:500.000*. DINAMIGE-M.I.E.M. Montevideo, 90 p.
- 1358 Preciozzi, F., Pena, S., Arrighetti, R. (1988a). *Memoria explicativa del fotoplano Isla Patrulla (E-19)*.
 1359 DINAMIGE - UdelaR, Montevideo, 13 p.
- 1360 Preciozzi, F., Pena, S., Arrighetti, R. (1988b). *Memoria explicativa del fotoplano Puntas del Yerbal (E-*
 1361 *18)*. DINAMIGE - UdelaR, Montevideo, 12 p.
- 1362 Preciozzi, F. (1989). *Memoria explicativa del fotoplano Zapicán (F-22)*. In: Carta Geológica del Uruguay.
 1363 DINAMIGE - UdelaR, Montevideo, 12 p.
- 1364 Rapela, C.W., Fanning, C.M., Casquet, C., Pankhurst, R.J., Spalletti, L., Poiré, D., Baldo, E.G. (2011).
 1365 The Rio de la Plata craton and the adjoining Pan-African/brasiliano terranes: their origins and
 1366 incorporation into south-west Gondwana. *Gondwana Research*, 20(4), 673-690.
- 1367 Reddy, S.M., Timms, N.E., Trimby, P., Kinny, P.D., Buchan, C., Blake, K. (2006). Crystal-plastic
 1368 deformation of zircon: a defect in the assumption of chemical robustness. *Geology*, 34:257-260
- 1369 Roberts, N.M., Spencer, C.J. (2015). The zircon archive of continent formation through time. *Geological*
 1370 *Society, London, Special Publications*, 389(1), 197-225.
- 1371 Rodríguez, P., Veroslavsky, G., Soto, M., Marmisolle, J., Gristo, P., de Santa Ana, H., Benvenuto, A.
 1372 (2015). New integrated Bouguer gravity anomaly map onshore Uruguay: preliminary implications for
 1373 the recognition of crustal domains. In: *SEG Technical Program, Expanded Abstracts* (pp. 1515-1519).
 1374 Society of Exploration Geophysicists.
- 1375 Rosière, C.A., Heimann, A., Oyhantçabal, P., Santos, J.O.S. (2018). The iron formations of the South
 1376 American platform. In *Geology of Southwest Gondwana* (pp. 493-526). Springer, Cham.
- 1377 Rubatto, D. (2017). Zircon: the metamorphic mineral. *Reviews in mineralogy and geochemistry*, 83(1),
 1378 261-295.
- 1379 Sánchez Bettucci, L., Preciozzi, F., Basei, M.A.S., Oyhantçabal, P., Peel, E., Loureiro, J. (2003).
 1380 Campanero Unit: a probable Paleoproterozoic basement and its correlation to other units of south-
 1381 eastern Uruguay. In: *IV South American Symposium on Isotope Geology, Short Papers*, 673-674,
 1382 CBPM; IRD, Salvador.
- 1383 Sánchez Bettucci, L., Peel, E., Oyhantçabal, P. (2010). Precambrian Geotectonic Units of the Río de Rio
 1384 de la Plata Craton. *International Geology Review*, 52(1), 32-50.
- 1385 Sánchez Bettucci, L., Loureiro, J., Demarco, P.N. (2021). Airborne geophysical characterization of
 1386 Uruguayan basement. *Journal of South American Earth Sciences*, 103206.

- 1387 Santos, J.O., Hartmann, L.A., Bossi, J., Campal, N., Schiprov, A., Theodoro, D., McNaughton, N.J. (2005).
 1388 Duration of the Trans-Amazonian Cycle and its correlation within South America based on U-Pb
 1389 SHRIMP geochronology of the La Plata Craton, Uruguay. *International Geology Review*, 45(1), 27-
 1390 48.
- 1391 Sato, K., Siga Jr, O., Nutman, A.P., Basei, M.A.S., McReath, I., Kaulfuss, G. (2003). The Atuba complex,
 1392 Southern South American platform: Archean components and Paleoproterozoic to Neoproterozoic
 1393 tectonothermal events. *Gondwana Research*, 6(2), 251-263.
- 1394 Sato, K., Basei, M.A.S., Siga Júnior, O., Sproesser, W.M., Onoe, A.T. (2009). Excimer laser (193 nm)
 1395 acoplado ao ICP-MS Neptune: primeiros resultados de análises isotópicas. In: *Simpósio 45 Anos de*
 1396 *Geocronologia no Brasil*. Resumos Expandidos, 131-133, USP.
- 1397 Schaltegger, U., Fanning, C.M., Günther, D., Maurin, J.C., Schulmann, K., Gebauer, D. (1999). Growth,
 1398 annealing and recrystallization of zircon and preservation of monazite in high-grade metamorphism:
 1399 conventional and in-situ U-Pb isotope, cathodoluminescence and microchemical evidence.
 1400 *Contributions to Mineralogy and Petrology*, 134(2-3), 186-201.
- 1401 Schaltegger, U., Davies, J.H. (2017). Petrochronology of zircon and baddeleyite in igneous rocks:
 1402 Reconstructing magmatic processes at high temporal resolution. *Reviews in Mineralogy and*
 1403 *Geochemistry*, 83(1), 297-328.
- 1404 Scherer, E.E., Whitehouse, M.J., Munker, C. (2007). Zircon as a monitor of crustal growth. *Elements*,
 1405 3(1), 19-24.
- 1406 Şengör, A.M.C., Dewey, J.F. (1990). Terranology: vice or virtue? *Philosophical Transactions of the Royal*
 1407 *Society of London. Series A, Mathematical and Physical Sciences*, 331(1620), 457-477.
- 1408 Siga Jr, O., Basei, M. S., Neto, J.R., Machiavelli, A., Harara, O.M. (1995). O Complexo Atuba: um
 1409 cinturão Paleoproterozoico intensamente retrabalhado no Neoproterozóico. *Boletim IG-USP. Série*
 1410 *Científica*, 26, 69-98.
- 1411 Silva Lara, H., Masquelin, H., Núñez Demarco, P. (2018). Formación Polanco: petrografía, estructura y
 1412 metamorfismo en la región de Polanco-Manguera Azul. *Revista Investigaciones*. Montevideo, 1(2),
 1413 17-29.
- 1414 Singh, V.K., Slabunov, A. (2016). Two types of Archaean supracrustal belts in the Bundelkhand Craton,
 1415 India: geology, geochemistry, age, and implication for craton crustal evolution. *Journal of the*
 1416 *Geological Society of India*, 88(5), 539-548.
- 1417 Stacey, J. T., Kramers, J.D. (1975). Approximation of terrestrial lead isotope evolution by a two-stage
 1418 model. *Earth and planetary science letters*, 26(2), 207-221.
- 1419 Tickyj, H., Hartmann, L.A., Vasconcellos, M.A.Z., Philipp, R.P., Remus, M.V.D. (2004). Electron
 1420 microprobe dating of monazite substantiates ages of major geological events in the southern Brazilian
 1421 shield. *Journal of South American Earth Sciences*, 16, 699-713.
- 1422 Tommasi, A., Vauchez, A., Fernandes, L.A., Porcher, C.C. (1994). Magma-assisted strain localization in
 1423 an orogen-parallel transcurrent shear zone of southern Brazil. *Tectonics*, 13(2), 421-437.
- 1424 UAF-NASA-JAXA (2011). ALOS Palsar RTC, Fine Dual Beam Polarization (FBD) data
 1425 coverage. (2011). PALSAR RT1 DEM, ASF, DAAC [<https://asf.alaska.edu>] [6/5/2015]. [doi:
 1426 10.5067/JBYK3J6HFSVF]
- 1427 Umpierre, M., Halpern, M. (1971). Edades Rb-Sr en rocas cristalinas del sur de la República Oriental del
 1428 Uruguay. *Revista de la Asociación Geológica Argentina*, Buenos Aires, 26(2): 133-151.
- 1429 Vavra, G., Gebauer, D., Schmid, R., Compston, W. (1996). Multiple zircon growth and recrystallization
 1430 during polyphase Late Carboniferous to Triassic metamorphism in granulites of the Ivrea Zone
 1431 (Southern Alps): an ion microprobe (SHRIMP) study. *Contributions to Mineralogy and Petrology*,
 1432 122(4), 337-358.
- 1433 Vavra, G., Schmid, R., Gebauer, D. (1999). Internal morphology, habit and U-Th-Pb microanalysis of
 1434 amphibolite-to-granulite facies zircons: geochronology of the Ivrea Zone (Southern Alps).
 1435 *Contributions to Mineralogy and Petrology*, 134(4), 380-404.
- 1436 Vermeesch, P. (2018). IsoplotR: A free and open toolbox for geochronology. *Geoscience Frontiers*, 9(5),
 1437 1479-1493.

- 1438 Wayne, D.M., Shima, R. K. (1988). Physical and chemical response of zircon to deformation.
 1439 *Contributions to Mineralogy and Petrology*, 98(1), 109-121.
- 1440 Williams, I.S., Compston, W., Black, L.P., Ireland, T.R., Foster, J.J. (1984). Unsupported radiogenic Pb in
 1441 zircon: a cause of anomalously high Pb-Pb, U-Pb and Th-Pb ages. *Contributions to Mineralogy and*
 1442 *Petrology*, 88(4), 322-327.

1443 Highlights

- 1444 1) The Pavas Block is an Archean inlier locating within the Neoproterozoic orogenic collage of Uruguay.
 1445 2) It has a different Paleoproterozoic tectonic evolution from the neighbouring blocks (Villa Serrana to
 1446 the SE and Cerro Chato to the West) and represents a suspected terrane.
 1447 3) The Pavas Block has a ~3.3-2.8 Ga high-grade metamorphic granitic gneiss core, over-thrusted by a
 1448 Neoproterozoic/Siderian succession and surrounded by ~2.0-1.8 Ga metagranitoids of Archean protolith.
 1449 4) Its southern boundary is defined by the end of Neoproterozoic/Siderian succession and the
 1450 Mesoproterozoic Tapes Complex, which limits with the Villa Serrana Block.

1451 FIGURE CAPTIONS

1452 **Figure 1:** Geotectonic map: a) Location of South American cratons (Modify from Fernandes et al., 1995),
 1453 b) Location of Mantiqueira Province and study area in Southwestern Gondwana (Modify from Sato et al.,
 1454 2003), c) Relative setting of the Cerro Chato, Pavas and Villa Serrana Blocks between the Dom Feliciano
 1455 Belt and the Rio de la Plata Craton (Modify from Preciozzi et al., 1985).

1457 **Figure 2:** Regional Geological sketch of the Nico Pérez Terrane, showing the main structural features and
 1458 lithological units (Modify from Oriolo et al., 2019).

1460 **Figure 3:** Airborne total count radiometric map of the Precambrian central domain, combined with the
 1461 ALOS Palsar topographic shaded relief, presenting the main photo-lineaments (yellow lines) and
 1462 geological references. **Blocks:** PAT - Piedra Alta Terrane, CCB - Cerro Chato, PB - Pavas, VSB - Villa
 1463 Serrana, PET - Punta del Este Terrane; **Shear Zones:** (a) Sierra Ballena, (b) Sarandí del Yí, (c) Sierra de
 1464 Sosa, (d) Cerros Amaro, (e) Cerro Largo, (f) Puntas de Pan de Azúcar; **Brittle faults:** (1) Cuchilla Rosario,
 1465 (2) Cueva del Tigre, (3) Timote, (4) Chamamé, (5) Tupambaé, (6) Arbolito, (7) María Albina, (8)
 1466 Asperezas, (9) El Soldado; **Supracrustal remnants:** (I) La Pedrera, (II) Valentín, (III) Monzón, (IV) Nico
 1467 Pérez, (V) Aparicio, (VI) Cañada Rodolfo, (VII) Casupá Chico; **Granitoids:** SL – Santa Lucia Batholith,
 1468 LP - Las Palmas Granite, CE - Cerrezuelo Granite, Y - Yermal Granite, GU - Guazunambí Granite, Y –
 1469 Yermal, IL - Illescas.

1470

1471 **Figure 4:** Airborne magnetic data showing the dx1 horizontal derivative of the reduced to pole (RTP)
 1472 magnetic anomaly at 1000 meters. There is a uniform negative magnetic signature for the Pavas Block
 1473 except in the southern part due to many mafic dykes (Data from DINAMIGE; Bates et al., 2016). Most of

1474 the faults are in the TC radiometric map (Fig. 5) but highlighted the most magnetic importance (identifiers
1475 are like Fig. 3).

1476

1477 **Figure 5:** Th / U vs. $^{208}\text{Pb} / ^{206}\text{Pb}$ correlation diagram for the six zircon samples. Correlation coefficients:
1478 CNP13F: +1.000, CNP77: -0.159, Mi21: +0.298, Mi30: +0.585, Mi14: +0.573, Mi19B: +0.345.

1479

1480 **Figure 6:** Textural correlation of zircons between the analysed rocks; each file corresponds to one sample
1481 and shows the most prominent zircons (a, b, c, d) and their textural variations. Circles indicate the LA-
1482 ICPMS pit; Th/U values are next to the corresponding spot; scale bar is 50 μm .

1483

1484 **Figure 7:** Selected grains showing the different zircon textural patterns: a) CNP13F-1c; b) CNP77-2d; c)
1485 Mi21-4a; d) Mi30-5b; e) Mi14-3c; f) Mi19B-6b.

1486

1487 **Figure 8:** Bulk $^{207}\text{Pb}/^{206}\text{Pb}$ (a) and $^{206}\text{Pb}/^{238}\text{U}$ ages (b) on histogram and statistics for all samples; four
1488 maxima for: 1) 3.1-3.2 Ga, 2) 1.9-2.0 Ga, 3) 1.4-1.5 Ga and 4) 0.5-0.6 Ga. One division in the x-axis
1489 represents 500 Ma; the y-axis shows the frequency number of zircons.

1490

1491 **Figure 9:** Concordia plots of U-Pb isotopic analyses of zircon from Archean rocks of La China Complex:
1492 (a) Spot selection for Hbl-bearing orthogneiss CNP13F (n=16) and weighted mean central age diagram
1493 suggesting two age groups; (b) Discordia model-1 for the same rock showing a UI age of 3270.8 ± 7 Ma,
1494 and a Kernel density estimation (KDE) confirming three age peaks (n=24); (c) Concordia model for
1495 CNP13F zircons showing a protracted distribution with a central age, and the KDE; (d) Concordia ages of
1496 the composite augen gneiss and mylonite (CNP77), showing three age groups, and a KDE, confirming
1497 these three groups (n=27); (e) Isochron corrected Concordia age of the Hbl-bearing orthogneiss Mi21
1498 (n=6) that yields 3137.5 ± 4.4 Ma, and a KDE; (f) Discordia model-1 of the same orthogneiss that yields a
1499 UI= 2985.6 ± 4.9 Ma and LI= 1804 ± 17 , and the weighted mean age diagram showing 1800.3 ± 1.7 Ma.

1500

1501 **Figure 10:** Concordia plots of U-Pb isotopic analyses of zircon from Rhyacian migmatites and granites of
1502 Campanero Unit: (a) Concordia model of the Mi30 Bt-bearing migmatite adding a Stacey-Kramers
1503 correction for common Pb (n=10) that yields 3074 ± 6.9 Ma (inherited age); (b) Concordia model for the
1504 same rock in Tera-Wasserburg diagram ($^{207}/^{206}\text{Pb}$ vs. $^{206}\text{Pb}/^{238}\text{U}$) that yields 1839.6 ± 2 Ma (n=31); (c)
1505 Concordia diagram of the Mi4 migmatite showing the relationship of the zircon part and its corresponding
1506 age group; (d) Discordia model-1 for the inherited-zircon age group (n=11) that yields an UI = 2973 ± 15
1507 Ma and a LI = 1887 ± 28 Ma; (e) Discordia model-1 for the "magmatic and recrystallised" age group
1508 (n=14) in the same sample, yielding an UI= 1917 ± 13 Ma; the weighted mean age diagram below (n=32)
1509 suggest a step among zircons of 2.0 Ga and 1.9 Ga; (f) Discordia model-1 of the mylonitic granite (Mi19b)
1510 that yields an UI= 1987.3 ± 3.2 Ma (n=11), and below the Concordia model yielding 1999.6 ± 3.1 Ma
1511 (n=16) and showing the disturbance of magmatic zircons.

1512

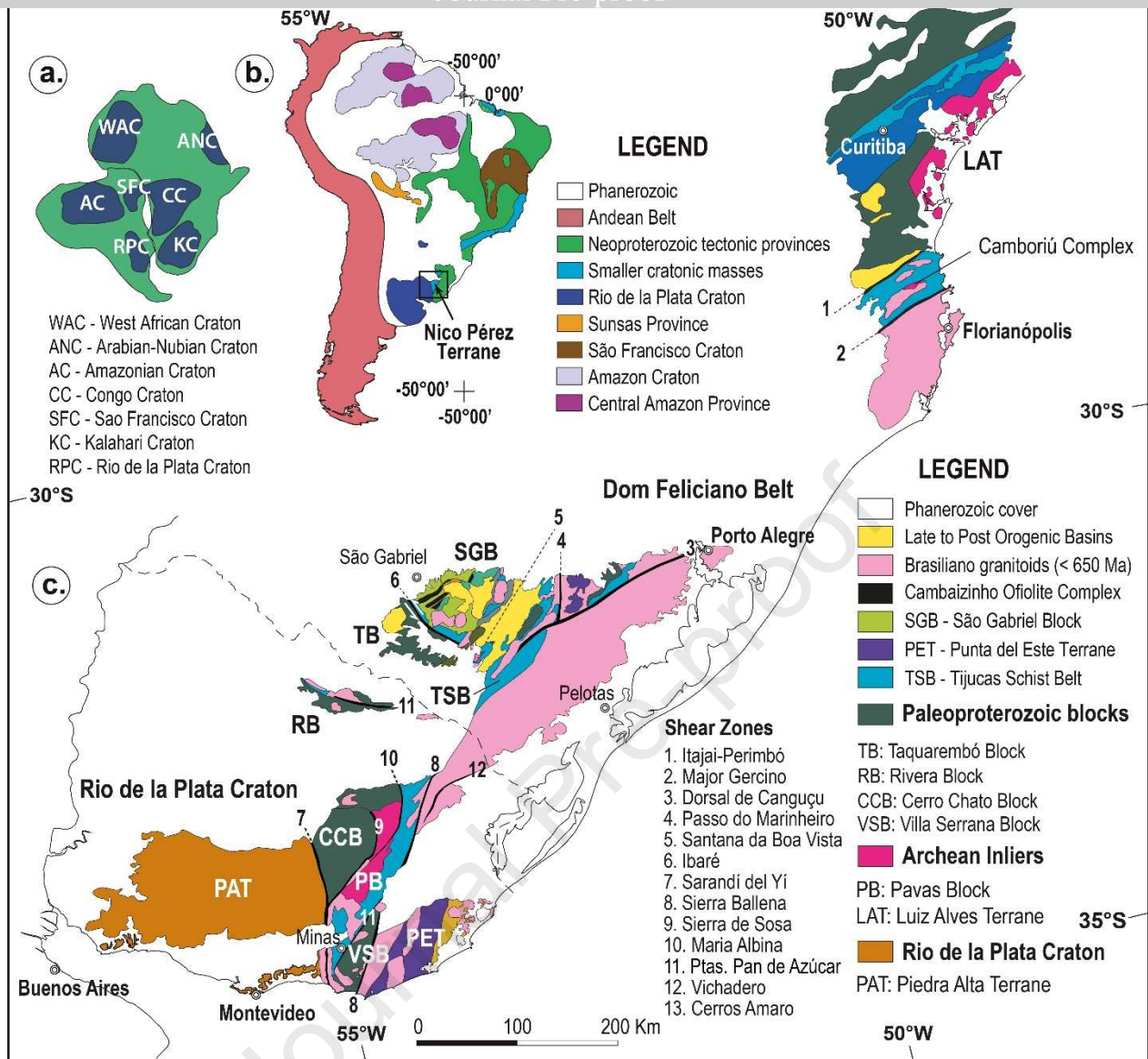
1513 **Figure 11:** Correlation of the Kernel Density Estimation about different Archean samples (Sample-1 of
1514 Hartmann et al., 2001; CNP13F, CNP77, Mi21, this work).

1515

1516 **Figure 12:** Geological and geophysical map integration showing the Nico Pérez Terrane and the Pavas
1517 Block's most relevant features. Structural-symbols' numbers correspond to the dips. The A-B profiles
1518 corresponds to Fig. 13.

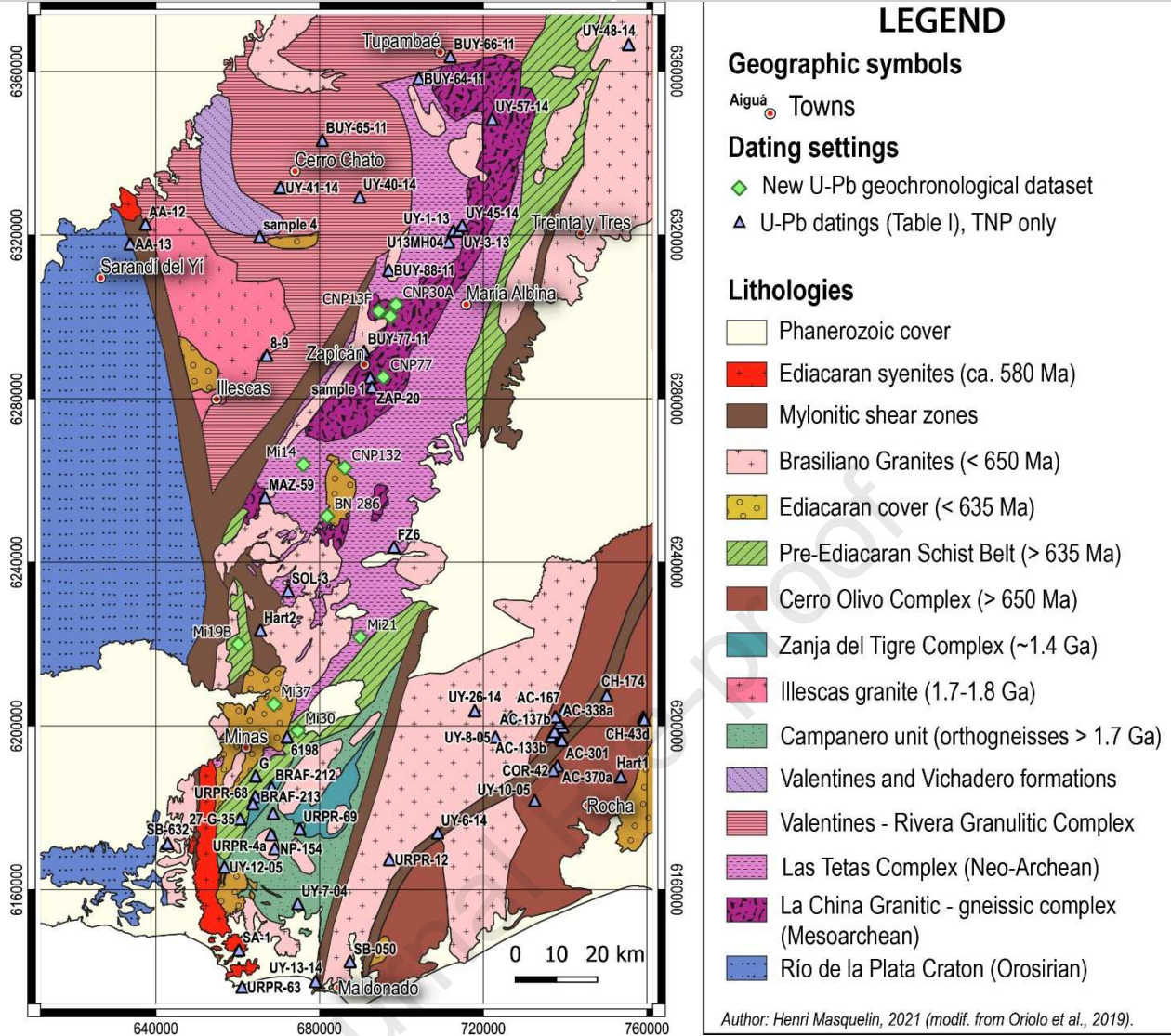
1519

1520 **Figure 13:** E-W geological profile cutting the different blocks within the Nico Pérez Terrane, up to the
1521 Neoproterozoic schist belt. The over-thrust of the Las Tetras Complex on La China Complex is presented.



1522
 1523
 1524

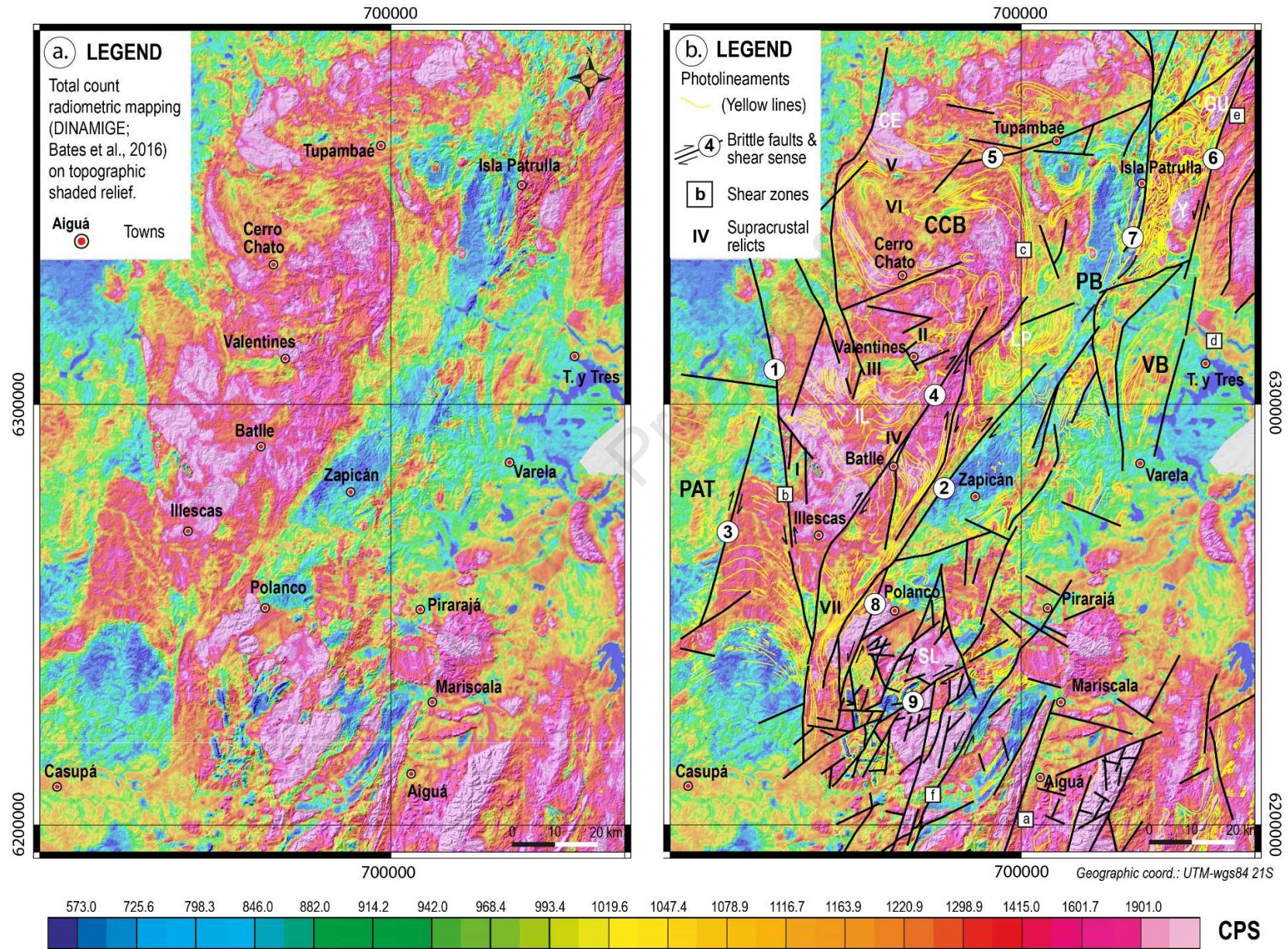
Figure 1



1525
1526
1527

Figure 2

528



529

530

Figure 3

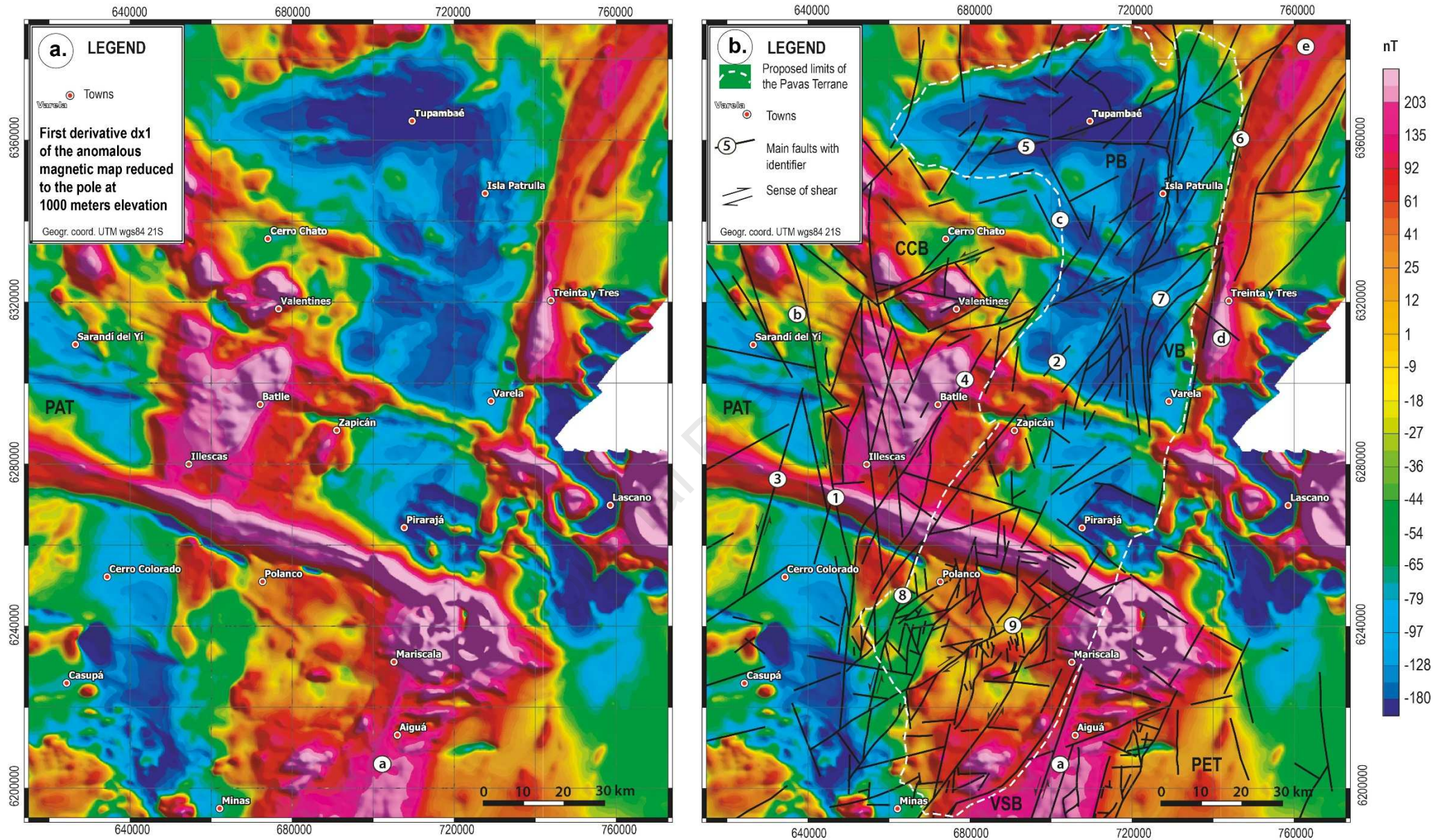
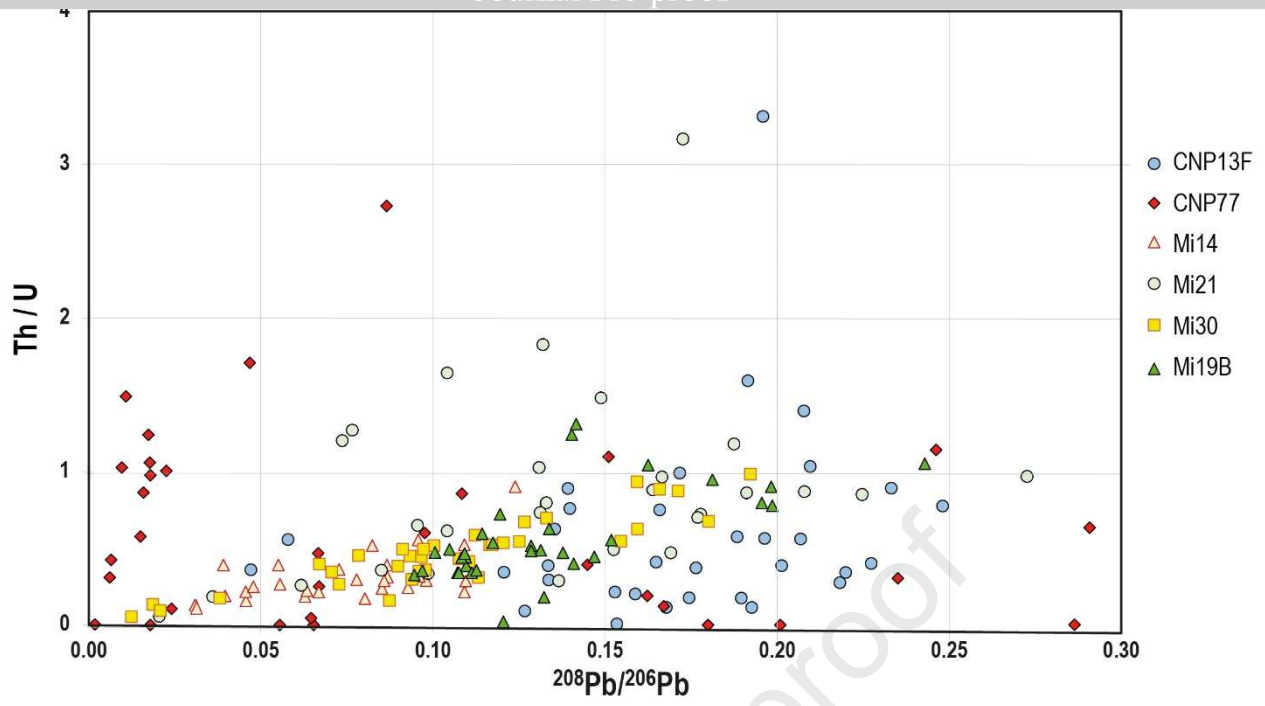


Figure 4

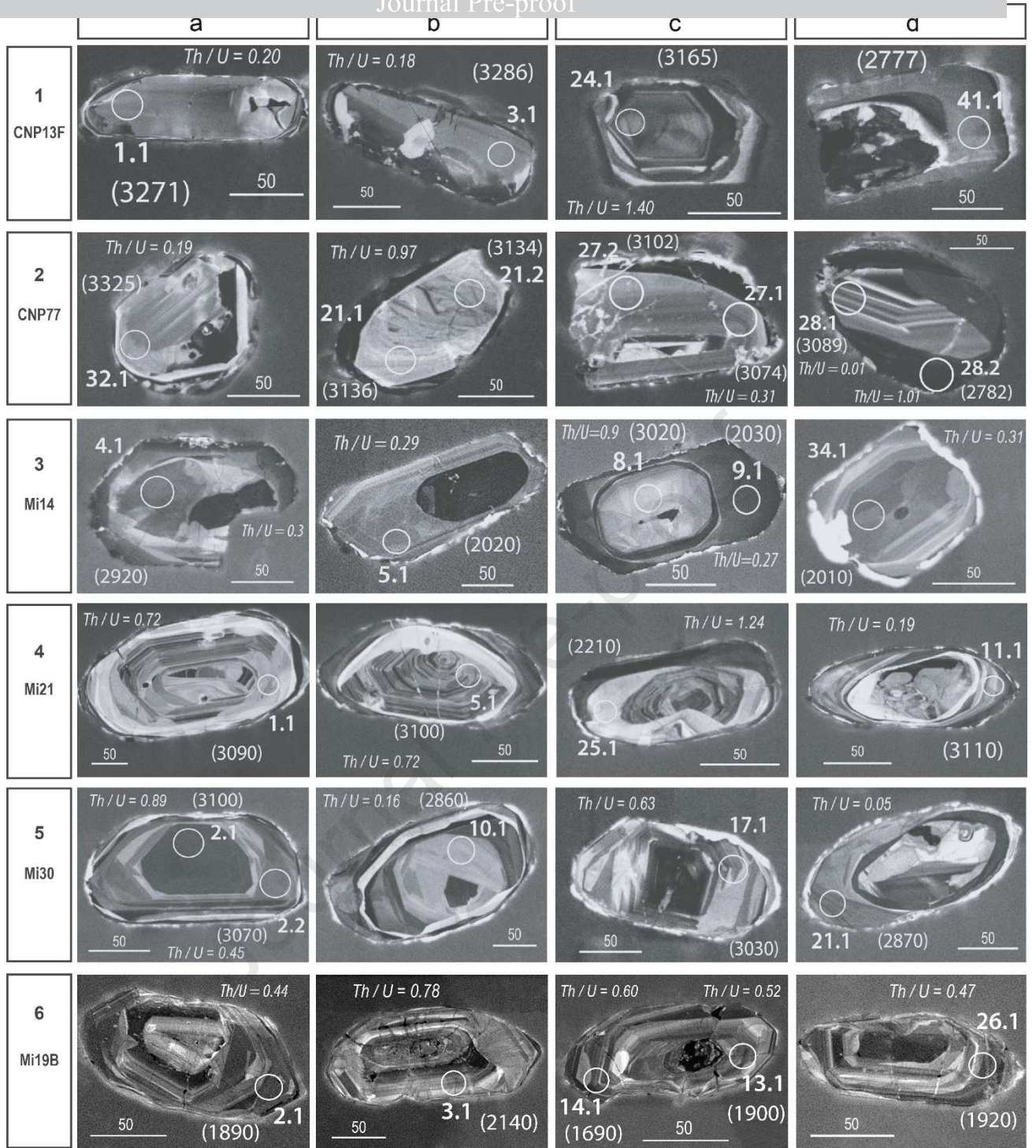
531
 532



1533

1534

Figure 5



1535
1536
1537
1538

Figure 6

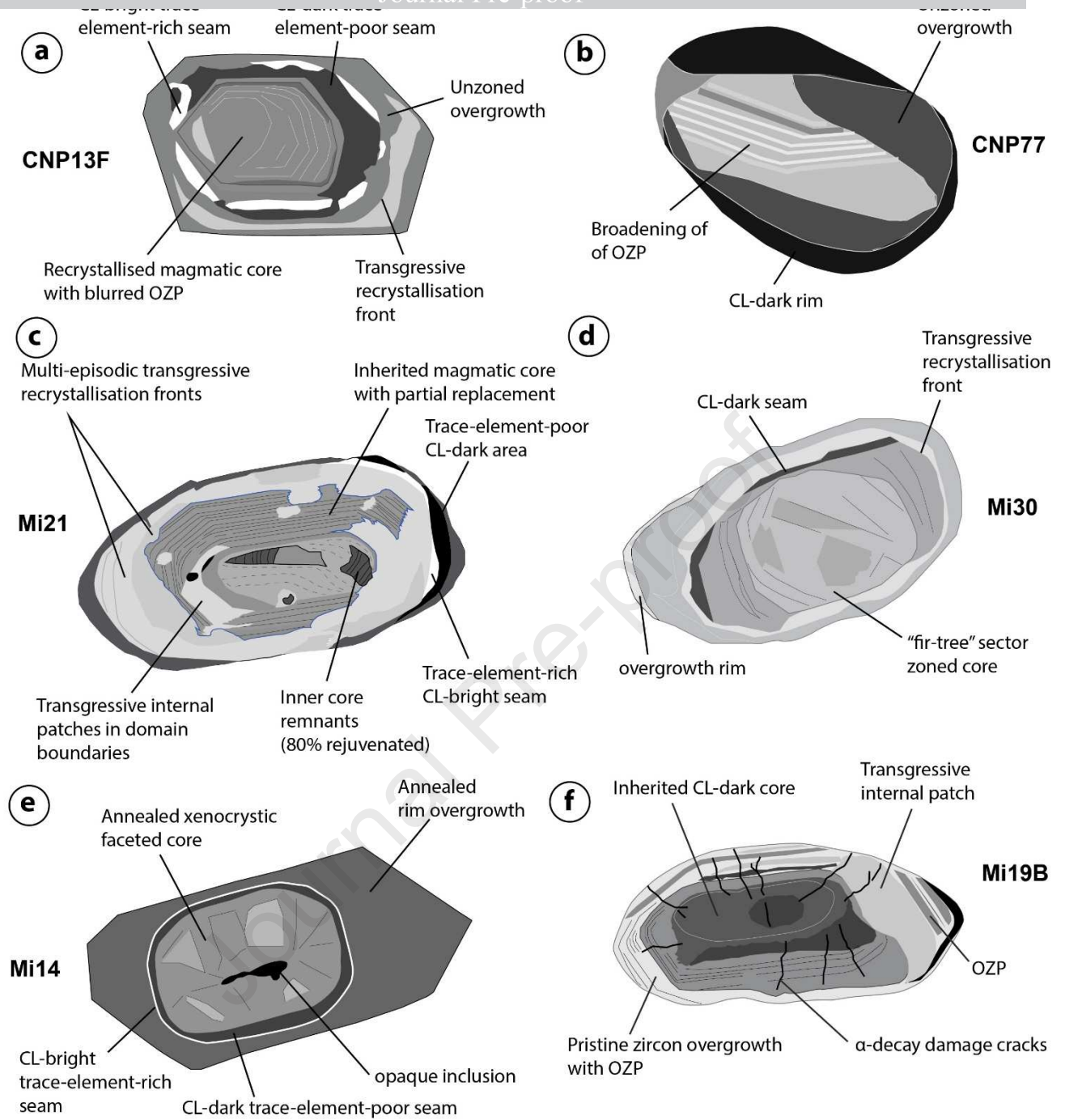


Figure 7

1539

1540

1541

1542

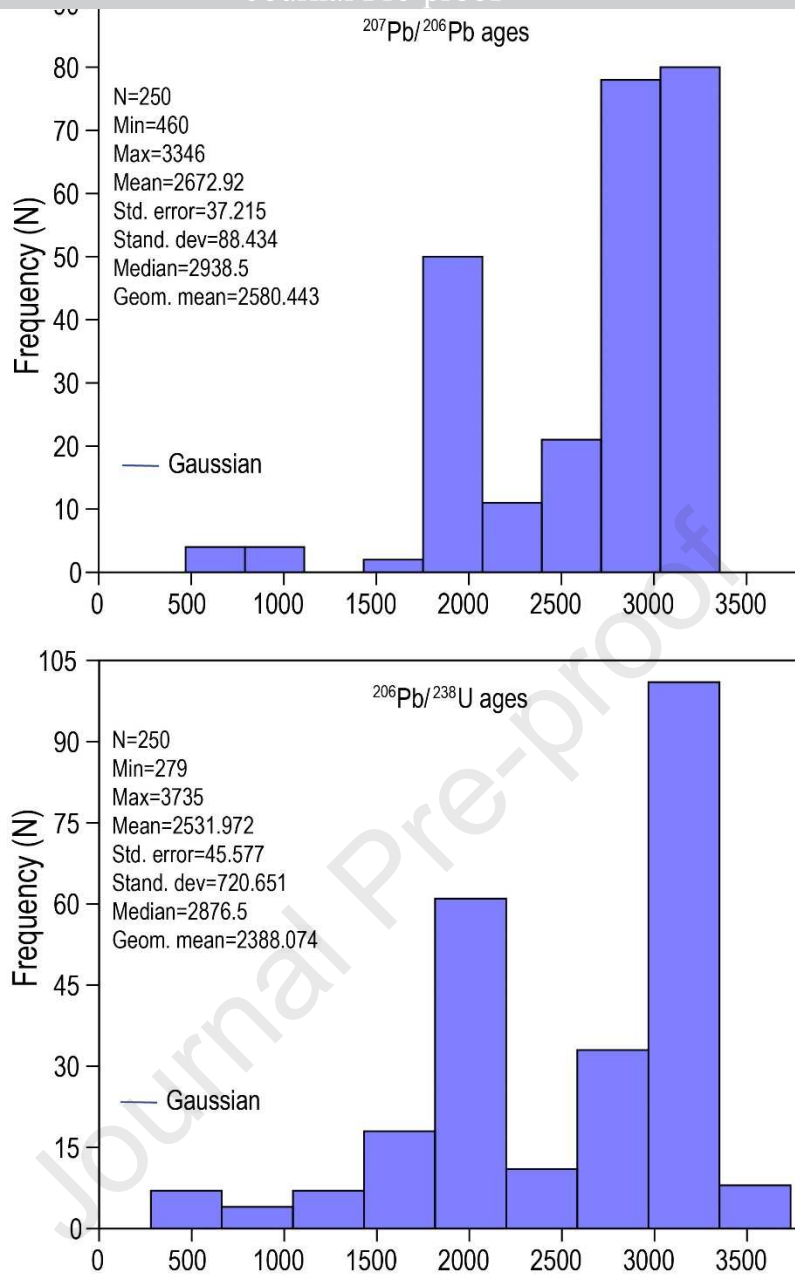


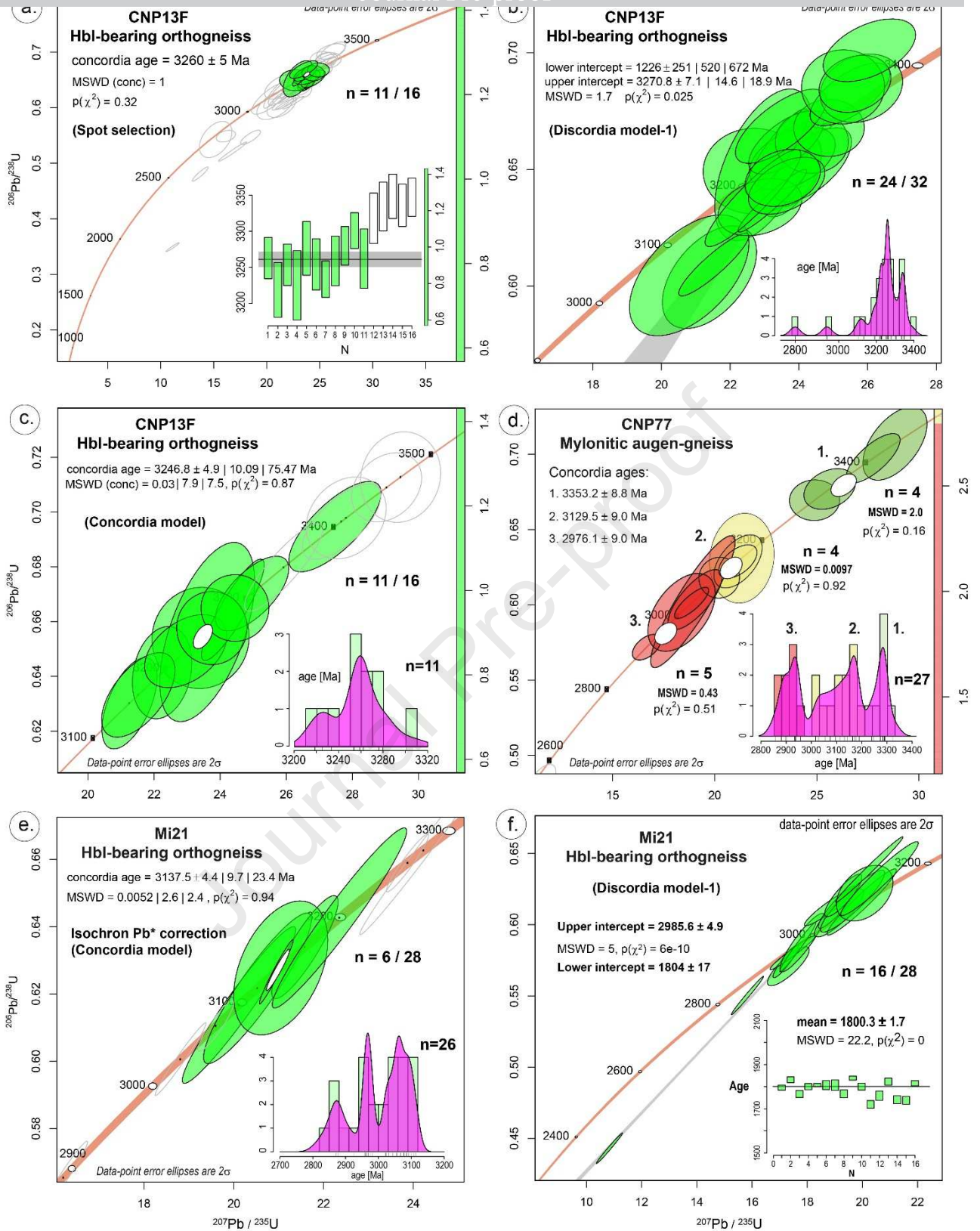
Figure 8

1543

1544

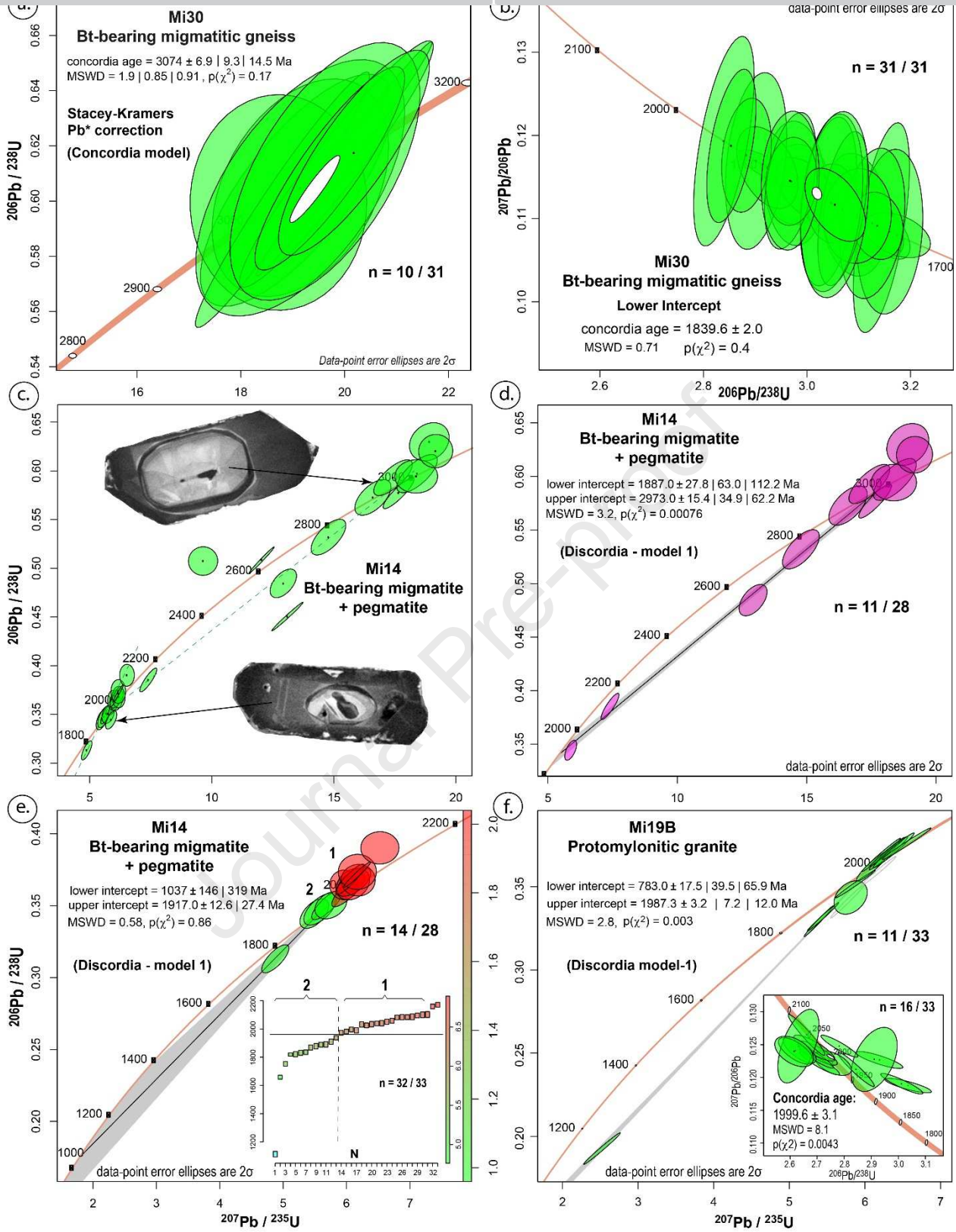
1545

1546



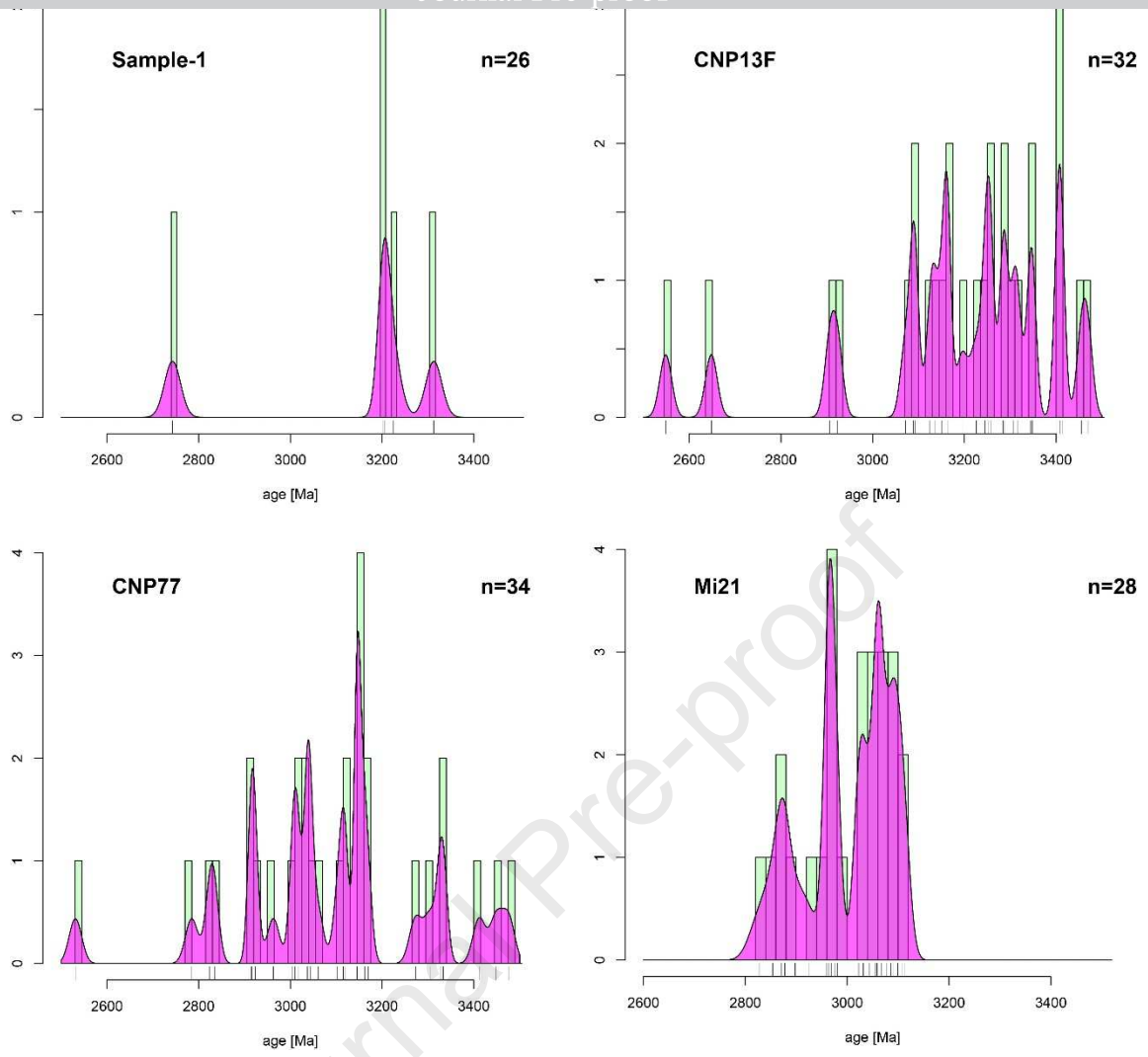
1547
 1548
 1549

Figure 9



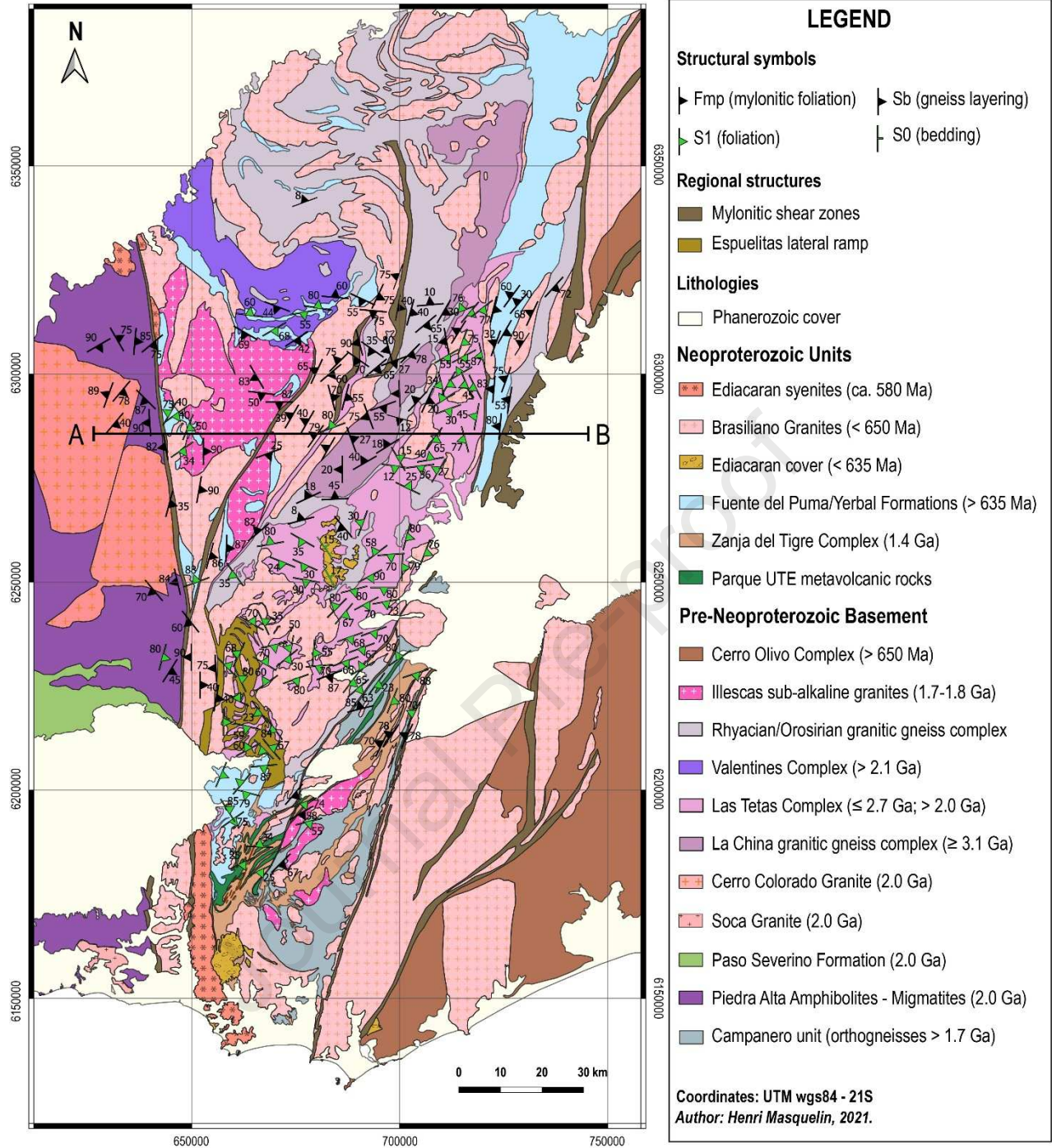
1550
 1551
 1552

Figure 10



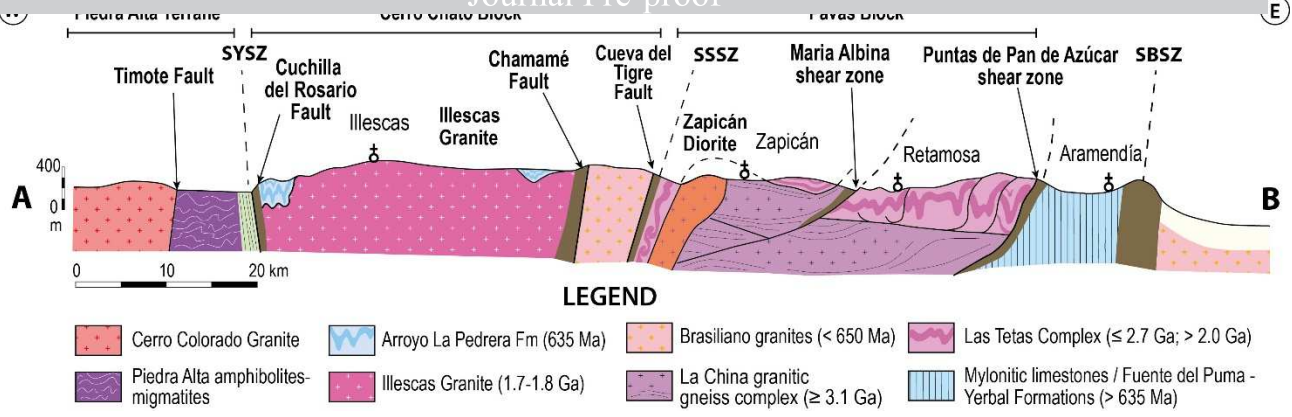
1553
1554
1555

Figure 11



1556
 1557
 1558

Figure 12



1559

1560

1561

Figure 13

HIGHLIGHTS

- The Pavas Block is an Archean inlier locating within the Neoproterozoic orogenic collage of Uruguay.
- It has a different Paleoproterozoic tectonic evolution from the neighbouring blocks (Villa Serrana to the SE and Cerro Chato to the West) and represents a suspected terrane.
- The Pavas Block has a ~3.3-2.8 Ga high-grade metamorphic granitic gneiss core, overthrust by a Neoproterozoic/Siderian succession and surrounded by ~2.0-1.8 Ga metagranitoids of Archean protolith.
- Its southern boundary is defined by the end of Neoproterozoic/Siderian succession and the Mesoproterozoic Tapes Complex, which limits with the Villa Serrana Block.

Personal Statement

I declare on my honor that this article has been written by me and my co-authors and does not contain any unpublished information unrelated to our research funded by the resources that have been provided by the funding institutions listed in the acknowledgments. Nor do we place a plagiarized copy of any document of another authorship.

Henri Masquelin.

2021 – 03 - 31

Declaration of interests

The authors declare that they have no known competing financial interests or personal relationships that could have appeared to influence the work reported in this paper.

The authors declare the following financial interests/personal relationships which may be considered as potential competing interests:

Journal Pre-proof